CHAPTER 3

BINARY AND TERNARY LAYERED DOUBLE HYDROXIDES (LDHs) FOR ADSORPTIVE REMOVAL OF VARIOUS ORGANIC DYE POLLUTANTS

This chapter of the thesis is divided into three sections demonstrating the complete characterization of various transition metal-based binary and ternary layered double hydroxides (LDHs) such as NiAl, NiMgAl and CuMgAl LDHs. The binary and ternary LDHs have been employed as adsorbent towards the removal of various organic dye pollutants from aqueous solution. Figure 3.1 shows the molecular structure of various organic dye pollutants used in the present investigation.

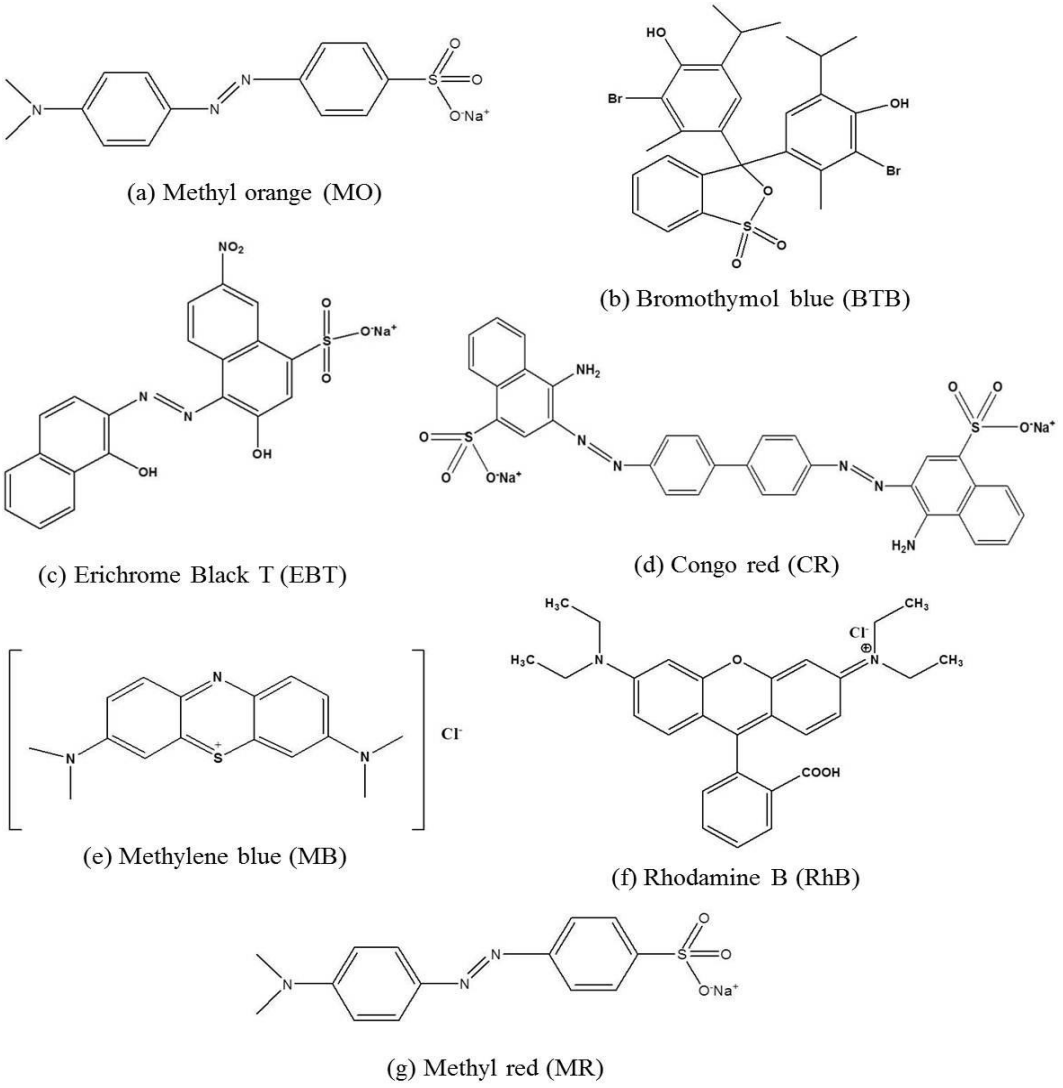

Figure 3.1. The molecular structure of various organic dye pollutants used in the present investigation.

3.1 Prologue

From the environmental point of view, the organic dye contaminants released from various sources such as textile, paper, painting, plastic, cosmetics, pharmaceutical and food industries have become the serious issue in all over the globe [1–4]. Disposal of the dye contaminants into the environment causes severe environmental pollution by contaminating soil and ground water, which adversely affect the human health as well as on aquatic life [5–9]. Due to their colorant nature, presence of even small quantity of dyes in water is highly visible to necked eye. It reduces the penetration of light and visibility through the water surface, effecting the photosynthetic cycle essential for the aquatic plants and also increases the chemical oxygen demand (COD) [10–12]. As a result, the aquatic plant and animals become unable to survive in that adverse situation. Synthetic origin and aromatic structure makes the dye molecules most stable and non-degradable in nature, due to which removal of dyes from waste water is not an easy task [13,14]. Some dyes are also toxic, mutagenic and carcinogenic in nature and therefore, their release into the environment is not acceptable at all [15–17]. Therefore, it needs to develop an efficient technique for removal of dye pollutants before being discharged into the environment.

Various techniques have been studied for removal of dyes from aqueous solution including coagulation [18], chemical oxidation [19], biodegradation [20–22] and photocatalysis [23–25]. The adsorption process is one of most reliable and widely adopted techniques with the advantages of simplicity, easy handing, economical feasibility and high efficiency [26–29]. Moreover, availability of various types of adsorbents makes the adsorption process as an efficient technique for dye removal. The use of different types of adsorbents such as activated carbon [30], fly ash [31], chitosan [32,33], zeolites [34] and clays [35–37] for removal of dyes from aqueous solution is well known. By virtue of the unique layered structure along with high surface area and anion exchange ability, LDHs have been extensively used as potential adsorbents towards the removal of organic dye pollutants [38–40].

Section 3A: Efficient removal of anionic organic dye pollutants from aqueous solution by NiMgAl layered double hydroxides

In this section, we have discussed the complete characterization of a series of NiMgAl LDHs with variable metal compositions synthesized via co-precipitation method. The synthesized LDHs have been employed as adsorbents towards the removal of anionic organic dye pollutants from aqueous solution. The synthetic procedures of NiMgAl LDHs with variable compositions, characterization technique details and adsorption methods are described in Chapter 2.

3A.1 Results and discussion

3A.1.1 Characterization of LDH samples

Figure 3A.1a shows the powder XRD patterns of the LDH samples. In all the cases, formation of sharp, intense peaks at low 2θ angles and broad, less intense peaks at higher 2θ angles reveal the formation of hydrotalcite–like LDH which match well with XRD database (JCPDS card no. 38−0478). The sharp peaks are observed approximately at 2θ = 11.6, 23.4 and 34.8° due to (003), (006) and (012) basal reflection planes, respectively and broad peaks are observed approximately at 2θ = 38.8, 46.3, 60.85 and 62.1° due to basal reflection planes of (015), (018), (110) and (113), respectively. As shown in figure, the peaks due to (003) and (110) reflection planes shifted slightly towards low 2θ angle with increasing Ni amount from LDH1 to LDH4. Figure 3A.1b clearly shows the close–up view of high 2θ angle for (110) reflection. Figure 3A.1c shows the intensity ratio of all the LDH samples at some 2θ angles. It is seen that the intensity decreases with increasing Ni amount from LDH1 to LDH4. However, LDH3 with Ni/Mg molar ratio 1:1 has comparatively higher intensity than LDH2 and LDH4. We have also calculated the % crystallinity of all the samples at some lower 2θ values (11.6, 23.4 and 34.8°) and they are shown in Figure 3A.1d. The result shows that the % crystallinity is highest for LDH3 compared to all other samples.

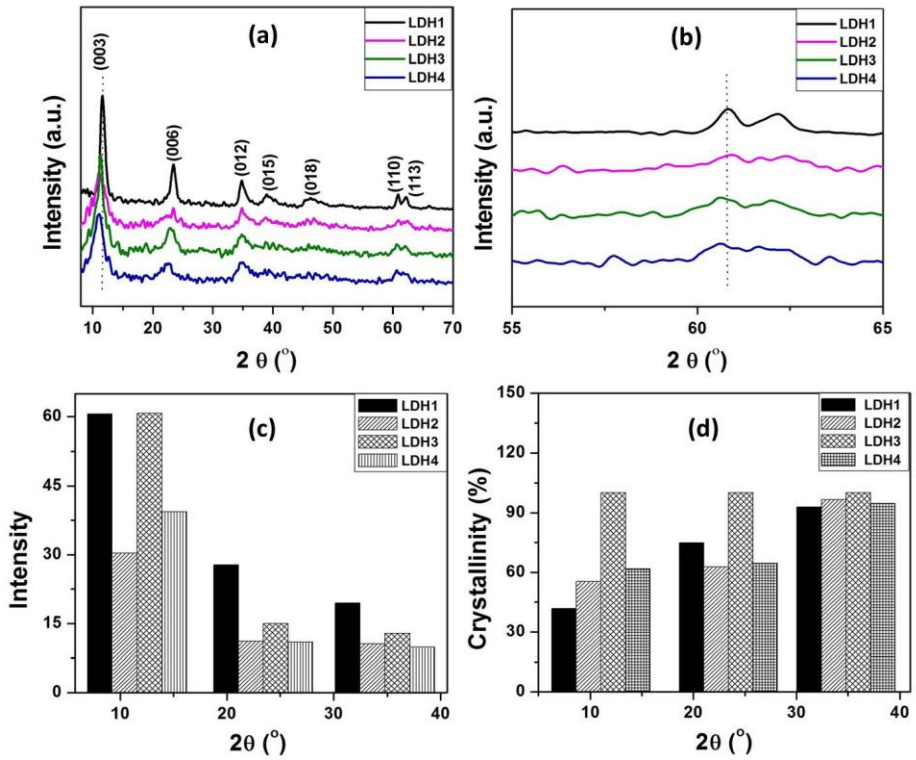

Figure 3A.1. (a) PXRD patterns and (b) High angle 2θ value, (c) Relative Intensity and (d) Crystallinity (%) at some 2θ angles of all the LDH samples.

The unit cell parameters *c* and *a* are calculated from (003) and (110) reflections using the equations, $c = 3d_{003}$ and $a = 2d_{110}$, respectively and their relationship with Ni/Mg molar ratio are shown in Figure 3A.2.

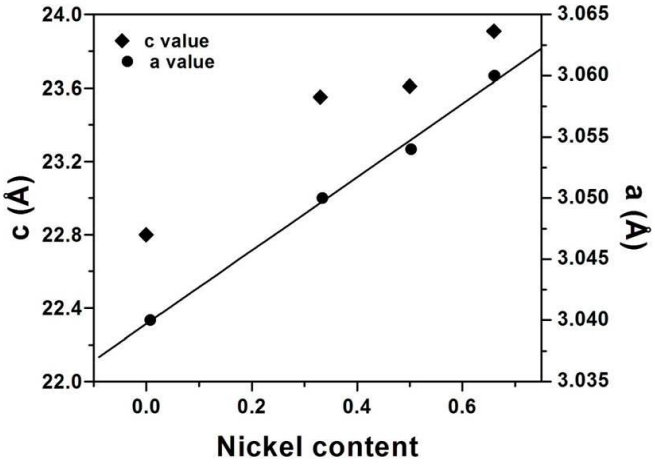

Figure 3A.2. Relationship of nickel content with unit cell parameters in LDH samples.

The *d* values of (003) and (110) reflections are also calculated using Bragg's equation, $2d\sin\theta = n\lambda$; where *d* is interplanar distance, θ is Bragg diffraction angle, λ is wavelength of X-ray and *n* is positive integer. The calculated cell parameters and *d* values are summarized in Table 3A.1. It is seen that cell parameter *a* increases gradually with increasing the Ni amount from LDH1 to LDH4 (Figure 3A.2, Table 3A.1). As cell parameter *a* is related to the distance of metal ions within the layers, incorporation of Ni in MgAl LDH increases the metal–metal distance resulting increase in cell parameter *a*. Again, the cell parameter *c* also gradually increases with increase in Ni amount from LDH1 to LDH4. The cell parameter *c* is related to the thickness of the brucite layer and the interlayer distance as a function of average charge of the metal cations, nature of the anion present in the interlayer region and water content present [41]. Ni^{2+} cation has larger ionic radius compared to that of Mg^{2+} cation. As the amount of Ni increases from LDH1 to LDH4, thickness and area of brucite layer increases and hence the cell parameter *c* is also increased. We have also calculated the crystallite sizes for (003) and (110) reflection planes and the calculated values are presented in Table 3A.1. Introduction of Ni in LDH also greatly affect the crystallite size. The calculated crystallite size gradually decreases with increasing Ni content from LDH1 to LDH4. However, the value is comparatively more in case of LDH3 compared to that of LDH2 and LDH4.

Table 3A.1. Elemental analyses, unit cell parameters and average crystallite sizes of the LDH samples.

LDH	**(Ni+Mg)/Al ratio**		d_{003} (Å)	d_{110} (Å)	**Unit cell parameters[b] (Å)**		**Crystallite size[c] (Å)**	
	Synthesized	**Analyzed[a]**			***c***	***a***	**(003)**	**(110)**
LDH1	0:3:1	0:3:0.9	7.69	1.52	23.07	3.04	90	134
LDH2	1:2:1	1:2:1	7.85	1.52	23.55	3.04	25.5	49.3
LDH3	1.5:1.5:1	1.5:1.47:0.9	7.87	1.53	23.61	3.05	63.5	113
LDH4	2:1:1	2:0.9:1	7.97	1.53	23.91	3.06	29.4	56.9

[a] Obtained from AAS analysis. [b] $a = 2d_{110}$, $c = 3d_{003}$. [c] Calculated using Debye-Scherer formula.

The elemental analyses of the as synthesized LDH samples are presented in Table 3A.1. The (Ni+Mg)/Al molar ratio of the analyzed samples are close to 3 which is nearly same as that of the synthesized LDH samples.

FTIR spectra of the LDH samples show absorption bands that are typical of layered materials (Figure 3A.3) [27]. A broad band is observed in the ranges of 3520 cm^{-1} for all cases and is assigned to the O–H stretching vibration of hydroxyl group of the layer and water molecule present in the interlayer region of LDH. The weak band observed around 1639 cm^{-1} is attributed to the bending vibrations of −OH group of interlayer water molecules of LDH. A sharp band is observed at around 1373 cm^{-1}, which is due to asymmetric stretching of CO_3^{2-} ion. Broad bands are observed at around 500−800 cm^{-1} (below 1000 cm^{-1}), due to the M−O−H and M−O−M vibrations [42].

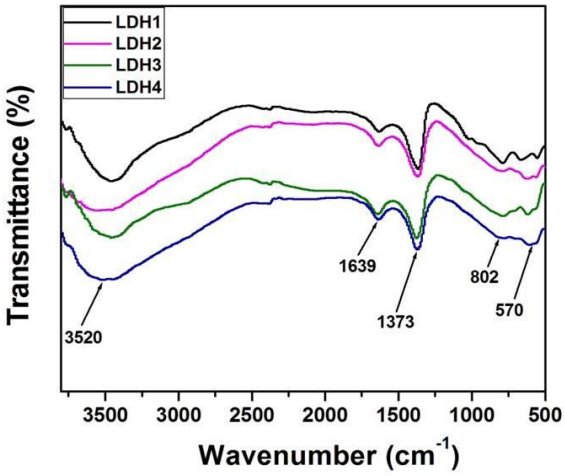

Figure 3A.3. FTIR spectra of the LDH samples.

Figure 3A.4a shows thermogravimetric analyses of the LDH samples. Mainly, two weight loss steps are observed that are typical of LDH materials. The first weight–loss step is observed due to the removal of water molecules adsorbed on the surface and in the interlayer region of LDHs in the temperature ranges of 50−200 °C. The second weight–loss step is observed due to the dehydroxylation of the brucite layer as well as the decomposition of the carbonate anions in the temperature ranges of 250−400 °C [43]. Figure 3A.4b shows the Raman spectra of LDH samples showing three characteristic Raman active modes (ν_1, ν_3 and ν_4) of carbonate intercalated LDH materials [44]. The

Raman spectrum of LDH1 shows a sharp, strong band at around 1060 cm^{-1} (ν_1 mode) and a weak ν_4 mode at 693 cm^{-1} due to the carbonate anions in the interlayer [45]. The broad band observed at 693 cm^{-1} is actually due to the overlapping of two bands at 682 and 697 cm^{-1} which are associated with M–OH bond of LDH layer and CO_3^{2-} anion in the interlayer region [44,46]. There is also a broad ν_3 mode band at around 1423 cm^{-1} but of very low intensity. The ν_2 mode is Raman inactive and therefore, it is not observed. It has also been observed that with increase in the Ni amount from LDH1 to LDH4, the intensity of ν_1 mode also gets increased and shifted to lower wavenumber. However, the intensity of ν_3 and ν_4 band gradually decreases with increase in amount of Ni from LDH1 to LDH4.

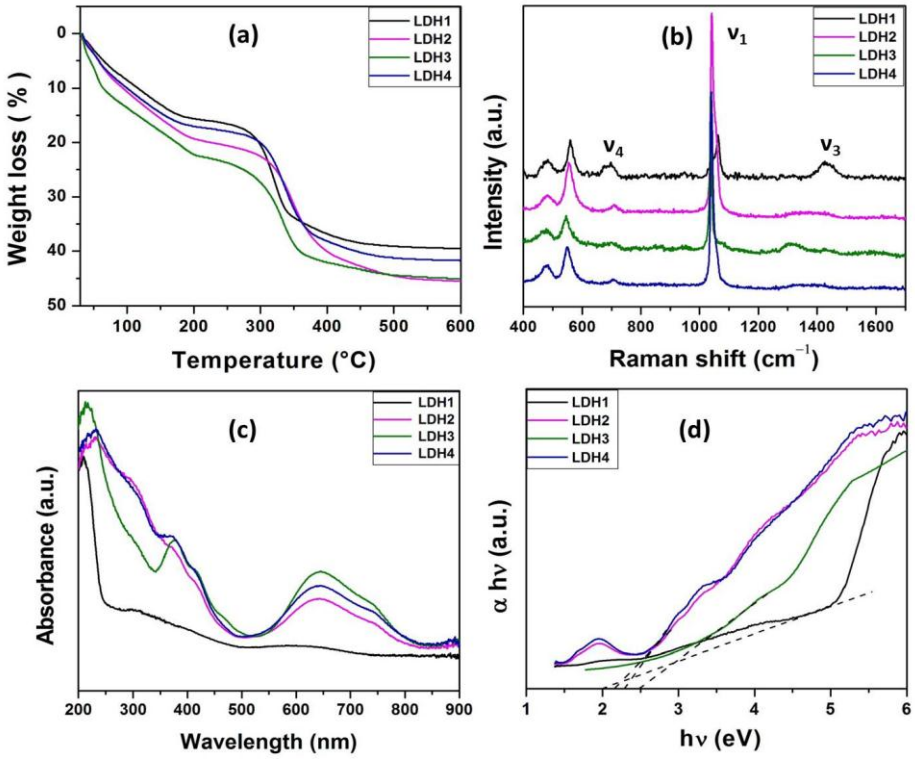

Figure 3A.4. (a) TGA graphs, (b) Micro–Raman spectra, (c) UV-vis DRS spectra and (d) Band gap energy calculated from UV-vis DRS of the LDH samples.

Diffuse–reflectance UV-vis spectroscopy was carried out to observe the visible light adsorption properties of the LDH samples and are shown in Figure 3A.4c. All the samples exhibit absorption band in the range of 200–300 nm, which is due to the ligand–to–metal charge transfer (LMCT) in the MO_6 octahedral of LDHs [43]. In case of LDH1, other peaks are not observed as both Mg and Al do not possess d electronic configuration.

Introduction of Ni in LDH1 gives rise to the formation of two peaks at 377 and 645 cm^{-1} along with two small weak peaks at 418 and 745 cm^{-1}. The peaks at 377 and 645 cm^{-1} are due to the allowed transitions of $^3A_{2g}$ (F) → $^3T_{1g}$ (P) and $^3A_{2g}$ (F) → $3T_{1g}$ (F) of d^8 Ni^{2+} cation [47]. The weak peaks are arises due to the spin-forbidden transitions, $^3A_{2g}$ (F) → ^1E_g (D) and $^3A_{2g}$ (F) → $^1T_{2g}$ (D) [47]. The peak intensity is also found to increase with increase in Ni content from LDH1 to LDH4 and it is highest for LDH3. The band gap energy (E_g) of LDH samples has been determined by using the Tauc/Davis–Mott expression as

$$(h\upsilon\alpha)^{1}/_{n_t} = A\left(h\upsilon - E_g\right) \quad (3A.1)$$

where, $h\upsilon$ is the energy of photon, α is the absorption coefficient, A is constant of proportionality and n_t denotes the characteristics of the transition in a semiconductor. For direct transition, value of n_t is 1 and for indirect transition, it is 4 [48]. In this case, the n_t value is 1 indicating a direct transition. The band gap energy (E_g) for all the LDH samples was calculated by extrapolating the curves to the x–axis (Figure 3A.4d) and values are given in Table 3A.2. The band gap energies (E_g) are increasing with increase in Ni amount in brucite layer from LDH1 to LDH4 and the value is highest for LDH3 (2.5 eV).

Table 3A.2. Band gap energy and textural properties of LDH samples.

LDH	Band gap energy[a] (eV)	S_{BET} (m^2/g)	Pore volume (cm^3/g)	Pore diameter (nm)
LDH1	2	131	0.16	3.88
LDH2	2.1	124	0.12	3.98
LDH3	2.5	268	0.27	3.70
LDH4	2.2	114	0.08	3.96

[a] Calculated from UV-vis DRS spectra.

The SEM images of the LDH samples show that flat plate–like shapes are observed for LDH1 (Figure 3A.5). However, agglomeration of the particles takes place on introduction of Ni in LDH due to which crystallites with large irregular particle size are observed for LDH2 to LDH4 (Figure 3A.5).

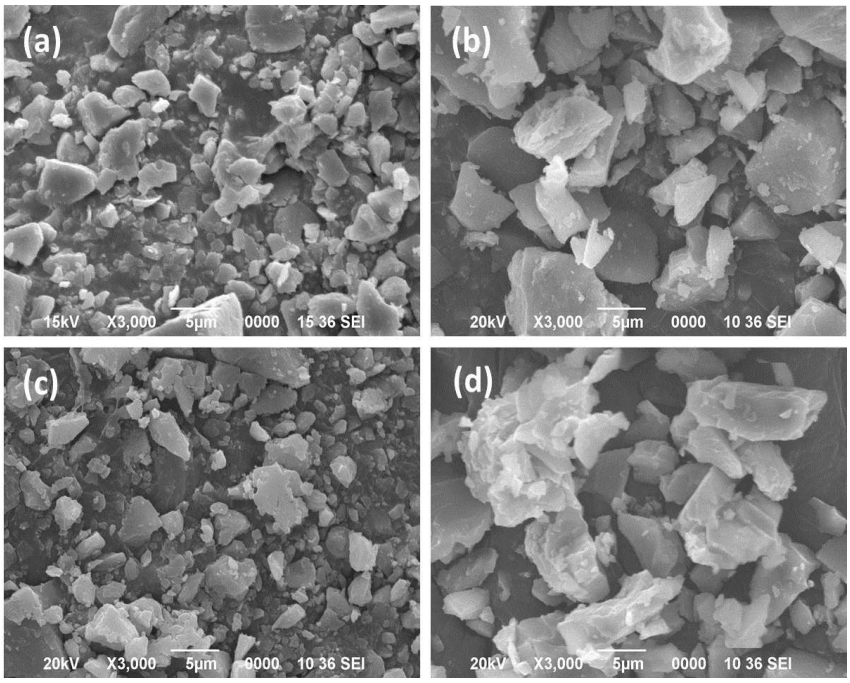

Figure 3A.5. SEM images of (a) LDH1, (b) LDH2, (c) LDH3 and (d) LDH4.

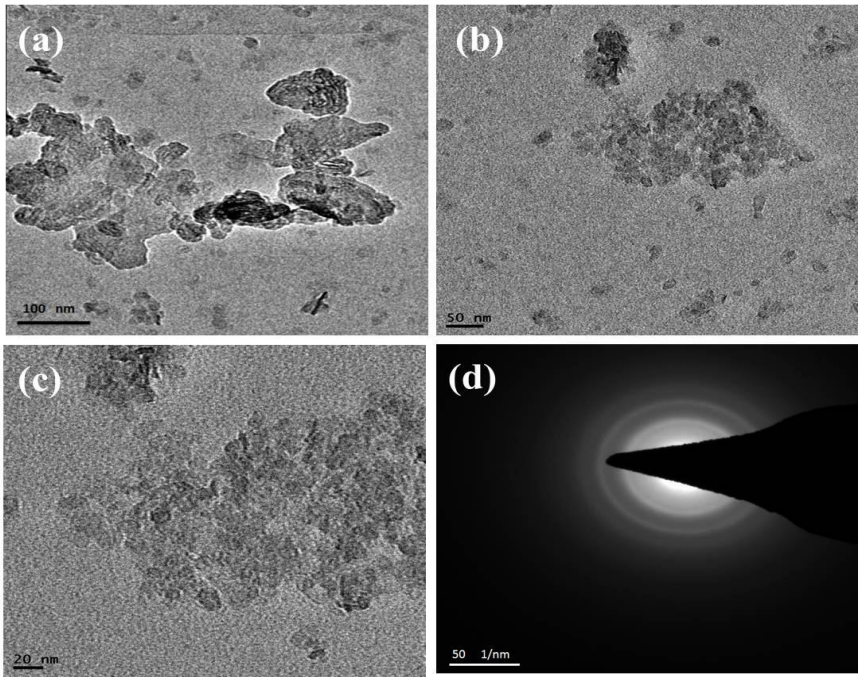

Figure 3A.6. TEM images at different resolution (a), (b) & (c) and SAED patterns (d) of LDH3.

TEM images of LDH3 at different resolution show that small, well dispersed particles with plate like morphology are observed (Figure 3A.6). The selected area

electron diffraction (SAED) pattern shows the presence of three concentric diffraction rings and the rings are due to (018), (110) and (113) lattice planes.

The porosity of the LDH samples was investigated using N_2 adsorption–desorption measurements. Figure 3A.7 shows the N_2 adsorption–desorption isotherms of various LDHs and insets are corresponding BJH pore size distribution plots. The N_2 adsorption–desorption isotherms of the entire LDH samples exhibit type IV isotherm typical of mesoporous materials [49]. LDH1 exhibits type IV isotherm with hysteresis loop of H3 type. However, LDH2, LDH3 and LDH4 display the type IV isotherm with hysteresis loop of H1 type which is the characteristic of mesoporous material with regular pore structure. The upper closer point of the hysteresis loop is appeared at a relatively higher value (P/P_o= 0.8) in case of LDH2, LDH3 and LDH4 samples than that of LDH1 (P/P_o= 0.5), demonstrating the highly porous nature of ternary LDHs.

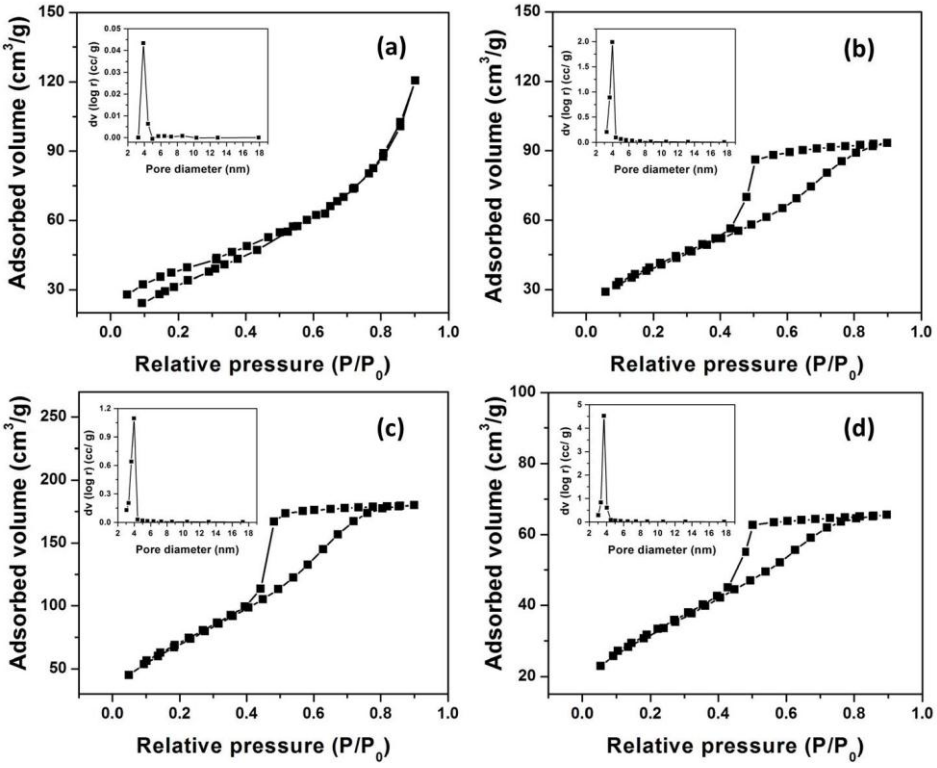

Figure 3A.7. N_2 adsorption-desorption isotherms and pore size distribution (inset) of (a) LDH1, (b) LDH2, (c) LDH3 and (d) LDH4.

All the LDH samples exhibit pore diameters in the ranges of 3.70–3.98 nm, characteristics of mesoporosity with a narrow unimodal pore size distribution curves (inset of Figure 3A.7). The BET surface areas and pore volumes of all the samples are calculated and presented in Table 3A.2. LDH1 possesses BET surface area and pore volume of 131 m^2/g and 0.16 cm^3/g, respectively. While the BET surface areas of LDH2, LDH3 and LDH4 are 124 m^2/g, 268 m^2/g and 114 m^2/g with pore volumes of 0.12 cm^3/g, 0.27 cm^3/g and 0.08 cm^3/g, respectively (Table 3A.2). LDH2 and LDH4 do not possess significant BET surface areas and pore volumes as LDH1. But LDH3 exhibits dramatically enlarged BET surface area and pore volume in comparison to LDH1. However, the calculated pore diameter of LDH3 is the lowest (3.70 nm) compared to the other three samples (Table 3A.2) which indicates that LDH3 is a highly porous materials with small pore diameter.

3A.1.2 Effect of contact time, adsorbent dosage, initial dye concentration and solution pH on adsorption of methyl orange (MO) onto LDH adsorbents

We carried out the adsorption experiment in a batch mode using 20 mL of 20 mg/L MO solution and 5 mg of the adsorbent at pH 6. Figure 3A.8a shows the effect of contact time on adsorption of MO onto various LDH samples. It is seen that for all cases, the adsorption of MO sharply increase within first 60–90 min to attain the equilibrium state and then proceeds slowly. The availability of the active free sites on the external surface of the adsorbent results in the fast adsorption of MO from solution within first 60–90 min. The result also shows the preferable and enhanced adsorption of MO on ternary LDHs (LDH2, LDH3 and LDH4) compared to binary LDH (LDH1). The % dye uptake of MO in case of LDH1 is 54%. While in case of LDH2, LDH3 and LDH4, the % dye uptakes are 96, 97 and 86%, respectively. Introduction of Ni in brucite-like LDH leads to the enhanced adsorption capacity for MO from LDH1 to LDH4. The molar ratio of Ni:Mg in ternary LDHs also has great impact on adsorption efficiency. LDH2 and LDH3 with molar ratio of Ni:Mg = 1:2 and 1:1 exhibit the highest adsorption capacity for MO compared to ternary LDH4. To determine the enhanced adsorption capacity of the ternary LDHs, we carried out the BET–surface area measurement of all the samples (Figure 3A.7 and Table 3A.2). The high BET surface area (268 m^2/g) and pore volume (0.27 cm^3/g) make the major contribution to the efficient adsorption capacity of LDH3 for MO.

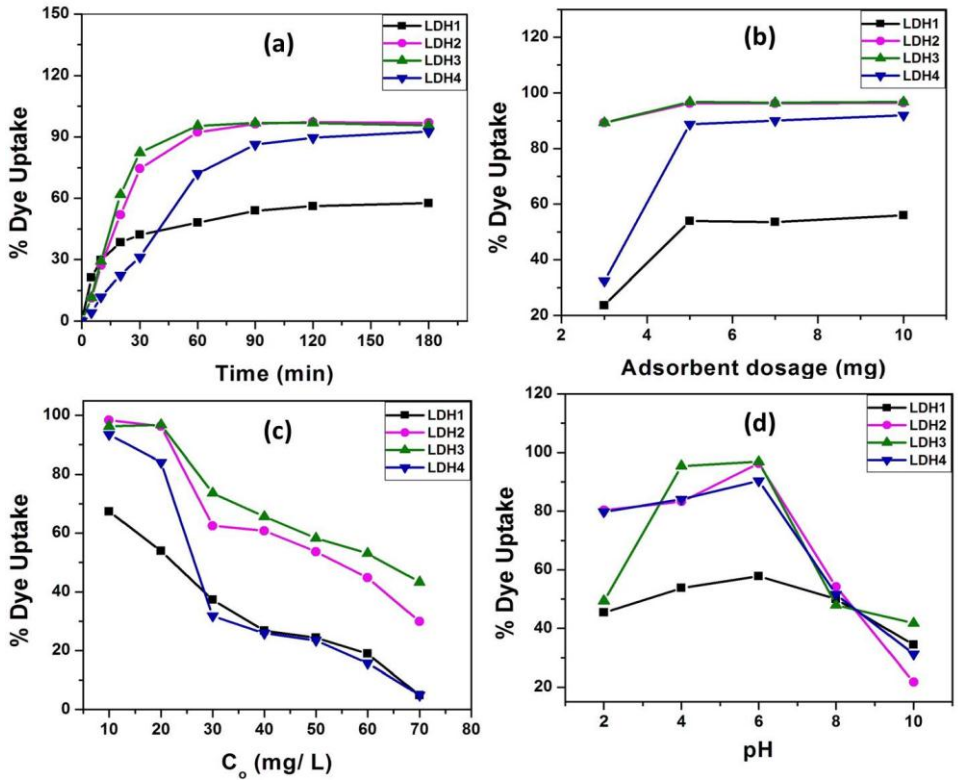

Figure 3A.8. Effect of (a) contact time, (b) adsorbent dosage, (c) initial dye concentration and (d) solution pH on adsorption of MO onto LDH adsorbents (Optimized adsorption conditions: MO concentration = 20 mg/L, adsorbent dose = 5 mg, equilibrium time = 90 min, pH = 6 and T = 25 °C).

However, for other two ternary LDHs (LDH2 and LDH4), although the BET surface areas are low compared to that of LDH1, the presence of Ni enhances the adsorption capacity for MO. Figure 3A.8b shows the effect of adsorbent dosages on adsorption of MO onto all the LDH adsorbents. The study was carried out using adsorbent dosages in the ranges of 3 to 10 mg with 20 mL of 20 mg/L initial MO concentration at pH 6. In all cases, a considerable increase in % dye uptake for MO has been observed on increase in the adsorbent dosage from 3 to 5 mg. Again, on increasing the adsorbent dosage from 5 mg upto 10 mg, no considerable increase in % dye uptake is observed. Saturation may arise due to the higher adsorbent amount, resulting in the decrease of % dye uptake. Moreover, at higher adsorbent dosages, agglomeration takes place due to collisions among the molecules resulting in the increase of diffusion path length and thus lowers the adsorption efficiency [27]. Therefore, 5 mg has been selected as an optimum adsorbent dosage for

further study as it gives a high % dye uptake even at a low adsorbent dosage. It is also clear from the figure that the % dye uptake of MO onto LDH2 and LDH3 is higher as compared to that of LDH1 and LDH4. Figure 3A.8c shows the effect of initial MO concentration on the adsorption process. We carried out the study with a series of MO solutions in the concentration range of 10–70 mg/L using 5 mg of the adsorbent for 90 min at pH 6. On increasing the initial MO concentration from 10 to 70 mg/L, a decrease in % dye uptake of MO is observed for all cases. This is due to the unavailability of the free adsorptive sites on the adsorbents after the adsorption of a fixed amount of dye concentration. The solution pH is an important parameter in adsorption process as it affects the adsorption of dye molecule by changing the surface charge as well as the active sites of the adsorbents and structure of the dye molecule. The effect of the solution pH on adsorption process was carried out at different pH ranges (pH 2 to pH 10). For all cases, the initial dye concentration and adsorbent dosage were kept constant at 20 mg/L and 5 mg. Figure 3A.8d shows the initial pH effect on adsorption of MO onto the LDH adsorbents. It is seen that for all cases, the % dye uptake is increased with increasing solution pH from 2 to 6 and again decreases gradually on increasing the pH from 6 to 10. The decrease in % dye uptake at low pH range (pH<4) is attributed to the dissolution of LDHs in highly acidic solution. The electrostatic attraction between the positively charged adsorbent surface sites and anionic MO dye, results in the enhanced adsorption of MO at pH range of 4–6. At higher pH (pH>6), negative charges may arises on the surfaces of the LDHs. These results in the electrostatic repulsion between the anionic MO dye and negatively charged adsorbent surface sites and hence, decrease in % dye uptake at pH above 6 [5]. Therefore, pH 6 has been selected as optimum pH of the MO solution for our study.

The corresponding UV-vis spectral changes for adsorption of MO for LDH1, LDH2, LDH3 and LDH4 adsorbents under optimized conditions are shown in Figure 3A.9.

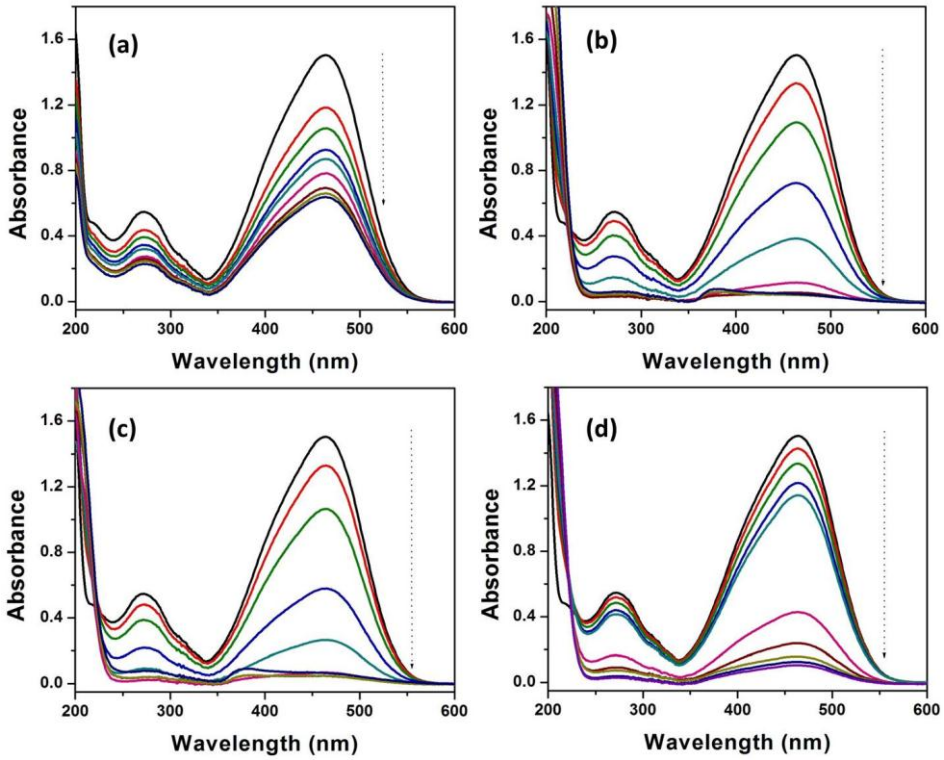

Figure 3A.9. UV-vis spectra for adsorption of MO onto (a) LDH1, (b) LDH2, (c) LDH3 and (d) LDH4 at various time intervals.

3A.1.3 Adsorption kinetics

To evaluate the adsorption kinetics of MO on LDHs, the experiments have been analyzed with pseudo-first and second order kinetic models using equations 2.6 and 2.7, respectively. The experimental data are plotted for both the kinetic models. Figures 3A.10 and 3A.11 shows the pseudo-first and second order kinetic plots for adsorption of MO onto various LDHs, respectively. The correlation coefficients (R^2), adsorption capacity (q_e and q_t) and rate constants (k_1 and k_2) values are calculated and listed in Table 3A.3. The kinetic data are fitted well with second order kinetic model with higher correlation coefficient (R^2) compared to that of first order kinetic model for all the cases. The R^2 values are 0.999, 0.999, 0.999 and 0.998 for LDH1, LDH2, LDH3 and LDH4, respectively. Thus, the adsorption process follows a pseudo second order kinetic model demonstrating the heterogeneous nature of the LDHs for MO.

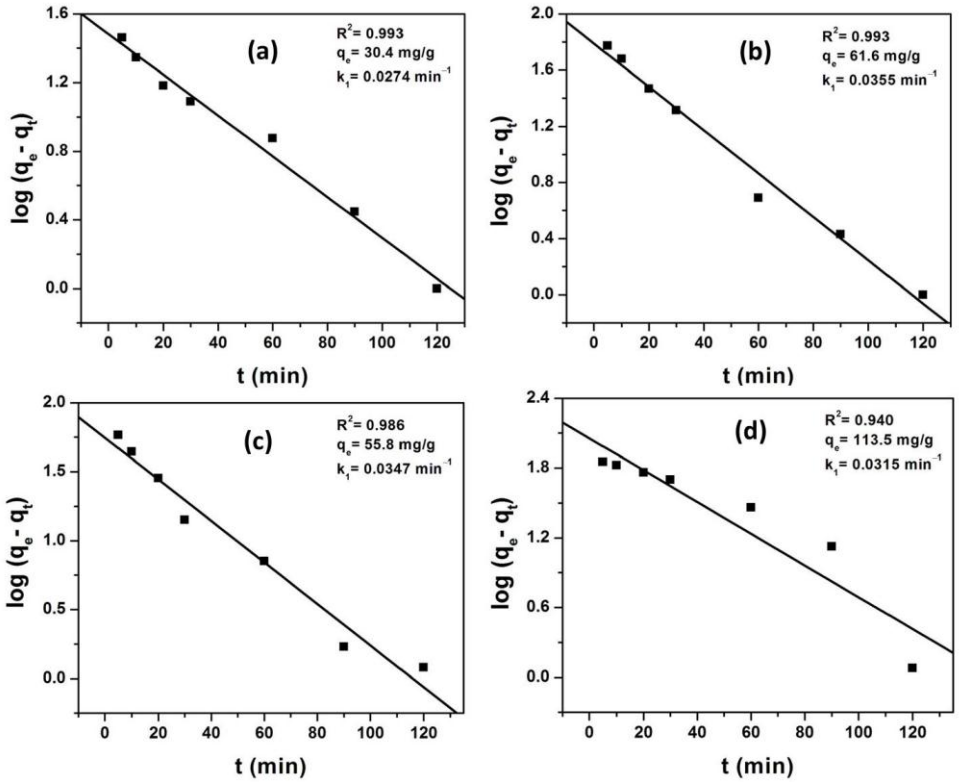

Figure 3A.10. Pseudo-first order kinetic plots for adsorption of MO onto (a) LDH1, (b) LDH2, (c) LDH3 and (d) LDH4.

Table 3A.3. Pseudo-first order and pseudo-second order kinetic parameters for adsorption of MO onto various LDHs.

LDH	**Pseudo-first order**			**Pseudo-second order**		
	q_e (mg/g)	k_1 (min^{-1})	R^2	q_e (mg/g)	k_2 (g/mg·min)	R^2
LDH1	30.4	0.0274	0.993	48.8	0.0017	0.999
LDH2	61.6	0.0355	0.993	85.8	0.0008	0.999
LDH3	55.8	0.0347	0.986	85.3	0.0009	0.999
LDH4	113.5	0.0315	0.940	190.1	0.00003	0.998

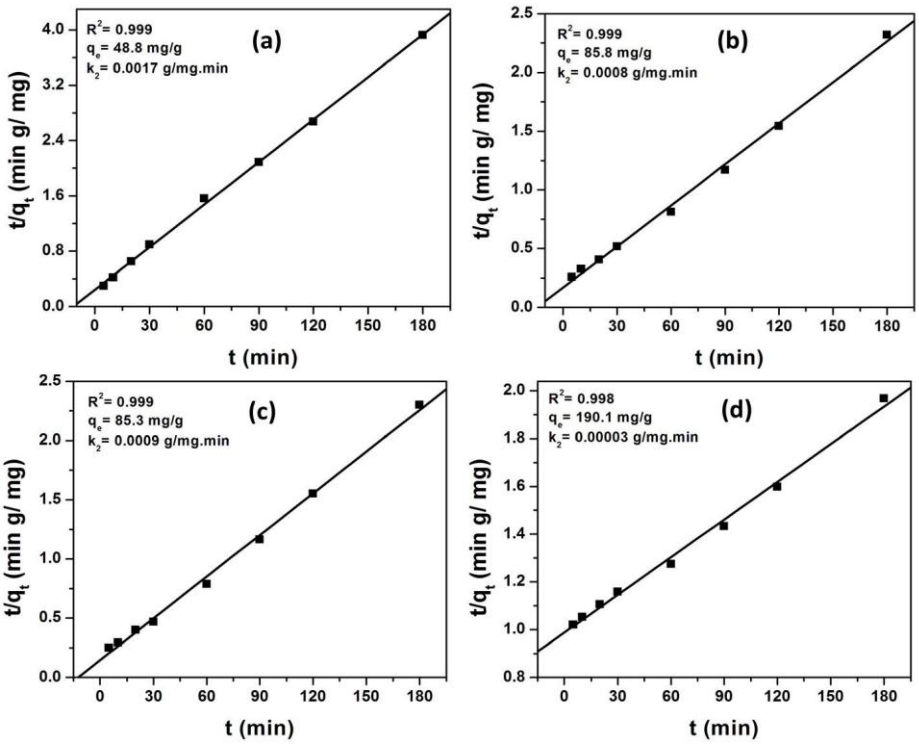

Figure 3A.11. Pseudo-second order kinetic plots for adsorption of MO onto (a) LDH1, (b) LDH2, (c) LDH3 and (d) LDH4.

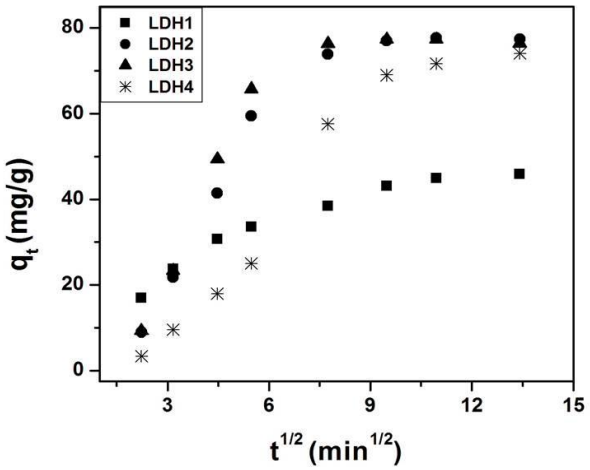

Figure 3A.12. Intraparticle diffusion plot for adsorption of MO onto the LDH samples.

The intraparticle diffusion kinetic model was taken into account to evaluate the diffusion mechanism of the adsorption process using equation 2.8. The plots of q_t versus $t^{1/2}$ for all the cases are linear curves and are not passing through the origin, indicating that the adsorption process is affected by more than one process (Figure 3A.12). The first

portion of the plot indicates that the adsorption of MO takes place on the external surface while the second portion indicates that the adsorption of MO takes place through the pores of the adsorbent (intraparticle diffusion) and the third portion of the plot implies the equilibrium stage [11].

3A.1.4 Adsorption isotherm

The adsorption isotherms have been analyzed with Langmuir and Freundlich isotherm models to illustrate the adsorption capacity at different equilibrium concentrations (equations 2.9 and 2.11, respectively). Figure 3A.13 and 3A.14 shows Langmuir and Freundlich isotherm plots for adsorption of MO onto various LDHs, respectively. The various isotherm parameters have been calculated from the Langmuir and Freundlich plots and are presented in Table 3A.4.

Table 3A.4. Langmuir, Freundlich and Dubinin–Radushkevich (D–R) isotherm parameters of MO onto various LDHs.

LDH	**Langmuir model**				**Freundlich model**			**D–R model**			
	R^2	k_L L/mg	q_m mg/g	R_L	R^2	k_F (mg/g) $(L/mg)^{1/n}$	n	R^2	k_{DR} mol^2/kJ^2	q_o mg/g	E kJ/mol
LDH1	0.987	0.551	37.6	0.1	0.845	17.8	5	0.917	2.24	36.5	0.473
LDH2	0.989	0.983	99.7	0.1	0.909	40.5	4	0.948	0.452	94.5	1.05
LDH3	0.999	0.483	127.9	0.1	0.983	55.4	4	0.929	0.386	111.8	1.14
LDH4	0.984	0.087	76.2	0.4	0.971	11.6	2	0.921	4.19	55.4	0.345

The experimental results show that based on the correlation coefficient (R^2) values, the adsorption data are fitted well with the Langmuir isotherm model compared to Freundlich isotherm model in all the cases indicating monolayer adsorption of MO dye on LDH surface. The ternary LDH3 possesses the highest value of maximum adsorption capacity, q_m (127.9 mg/g) compared to the other LDHs (Table 3A.4). The favorability of the adsorption process can be predicted from the value of dimensionless constant

separation factor or equilibrium parameter, R_L using equation 2.10. The calculated R_L value in our study is between 0 and 1 in all cases (Table 3A.4), thereby confirming that the adsorption process is a favorable one.

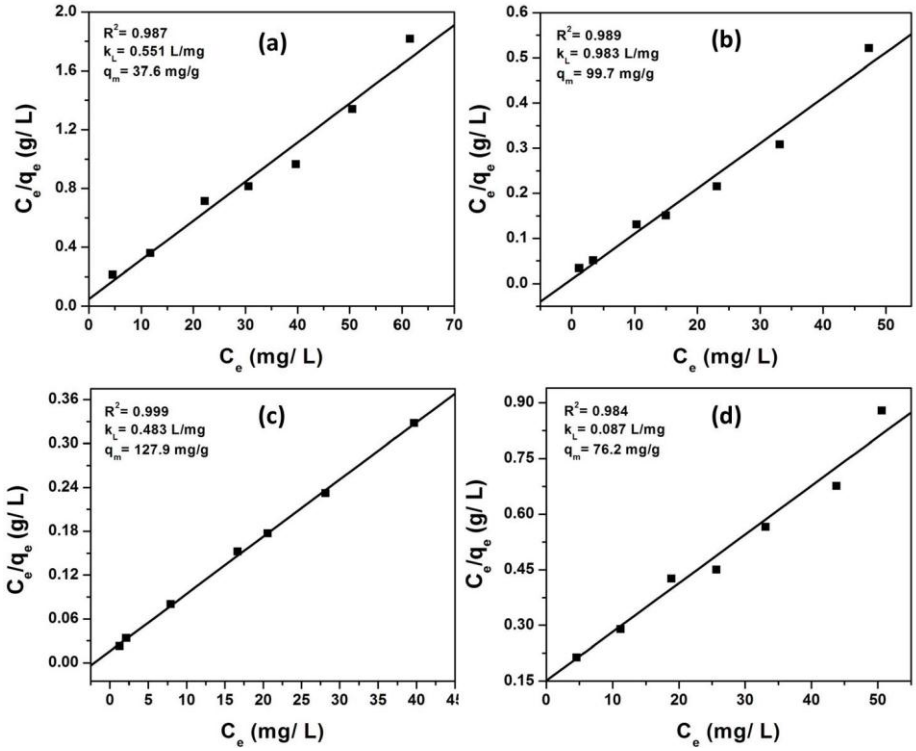

Figure 3A.13. Langmuir isotherm plots for the adsorption of MO onto (a) LDH1, (b) LDH2, (c) LDH3 and (d) LDH4.

Additionally, Dubinin–Radushkevich (D–R) isotherm model has been chosen to understand the adsorption mechanism to a deeper extend using equation 2.12. Various parameters are obtained from the linear plot of ln q_e versus ε^2 (Figure 3A.15) and presented in Table 3A.4. With the D–R isotherm model, the mean adsorption energy (E) values are also calculated using equation 2.14. The value of E between 1–16 kJ/mol prevails physical adsorption and the value more than 16 kJ/mol prevails chemisorptions [50]. From our experimental results, the E values obtained are 0.4730, 1.05, 1.14 and 0.3453 kJ/mol for LDH1, LDH2, LDH3 and LDH4, respectively (Table 3A.4). This implies that the process involved in the adsorption of MO onto LDH surfaces is the physical adsorption.

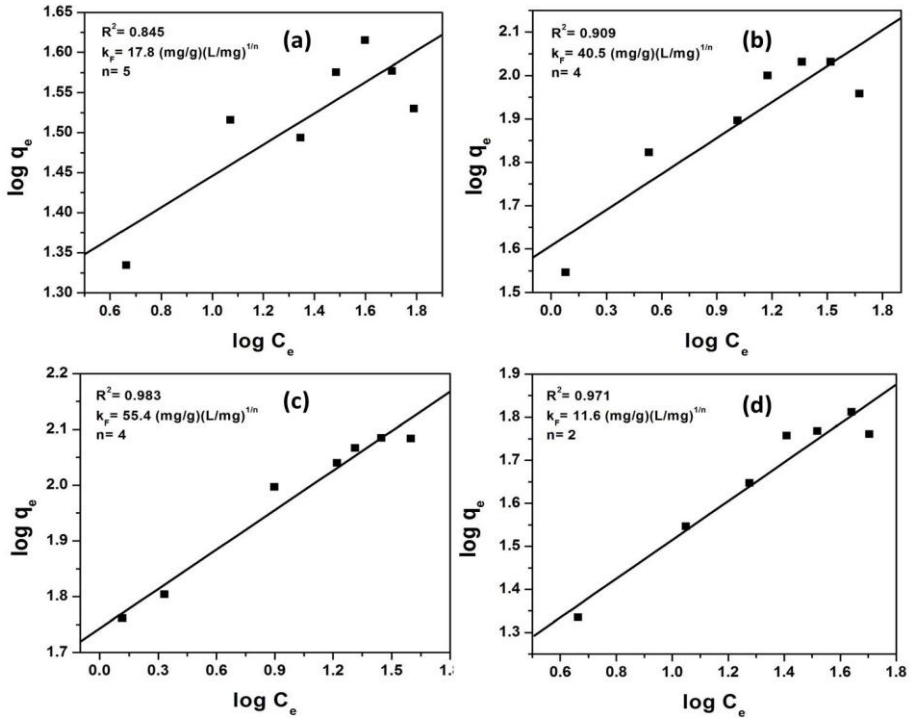

Figure 3A.14. Freundlich isotherm plots for the adsorption of MO onto (a) LDH1, (b) LDH2, (c) LDH3 and (d) LDH4.

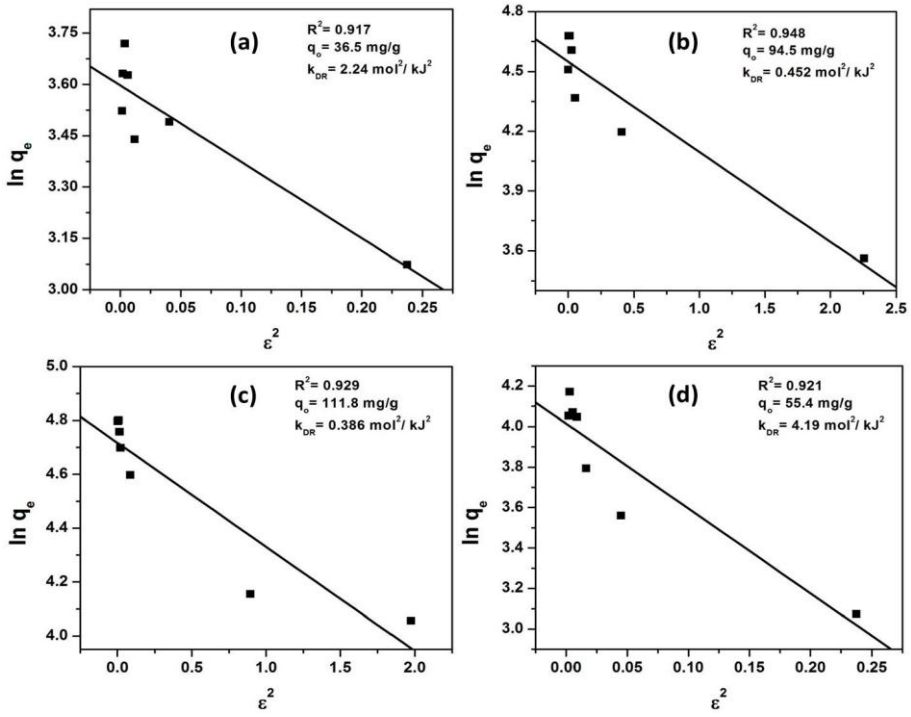

Figure 3A.15. D–R isotherm plots for adsorption of MO onto (a) LDH1, (b) LDH2, (c) LDH3 and (d) LDH4.

3A.1.5 Possible mechanism of adsorption

To understand the adsorption mechanism to a deeper extend, we have carried out XRD, FTIR and SEM analysis before and after adsorption of MO using the best adsorbent, LDH3. Figure 3A.16 shows the schematic diagram for efficient removal of anionic MO dye from aqueous solution over LDH3 adsorbent.

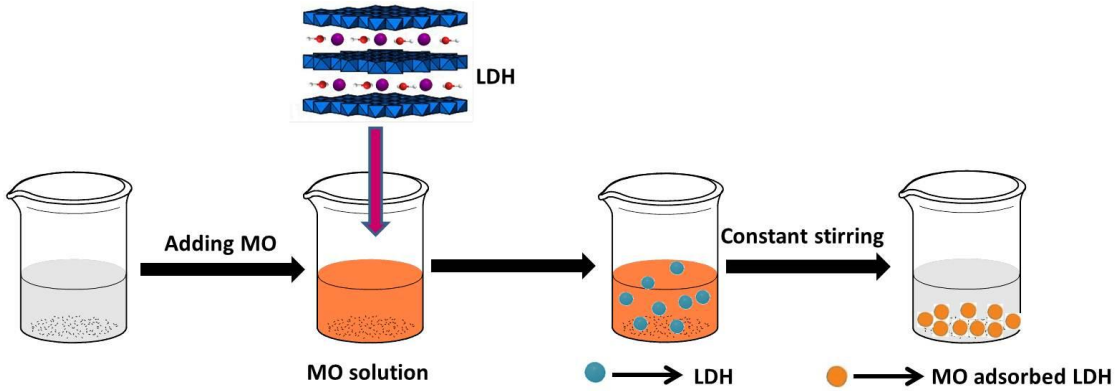

Figure 3A.16. Schematic diagram for efficient removal of MO over LDH3 adsorbent.

The corresponding UV-vis spectra of MO before and after adsorption on LDH3 is shown in Figure 3A.17a and inset of the figure shows the photograph of color change on adsorption. The characteristic adsorption peaks of MO disappear after adsorption onto LDH surface. From the photograph, it is also observed that the solution of methyl orange is changed to a colorless, clean solution after adsorption, indicating efficient adsorption of MO onto the LDH surface. The XRD patterns of LDH3 before and after adsorption of MO shows that no characteristic changes takes place on adsorption indicating retention of the layered structure after adsorption (Figure 3A.17b).

The morphological changes of the LDH before and after adsorption can be observed from the SEM images (Figure 3A.18). From the images, it is seen that no significant morphological change is observed after adsorption of MO onto LDH3 and this finding suggests that the LDH structure is retained after adsorption. However, a layer is appeared in the image, indicating the accumulation of dye over the surface of LDH adsorbent.

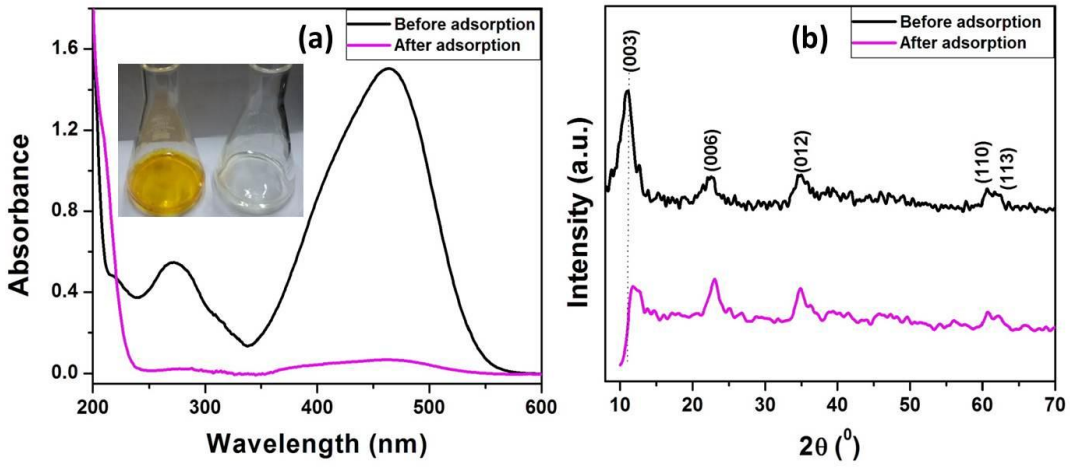

Figure 3A.17. (a) UV-vis spectra of MO before and after adsorption onto LDH3 and inset is photographs of MO before (left) and after adsorption (right), (b) XRD patterns of LDH3 before and after adsorption of MO.

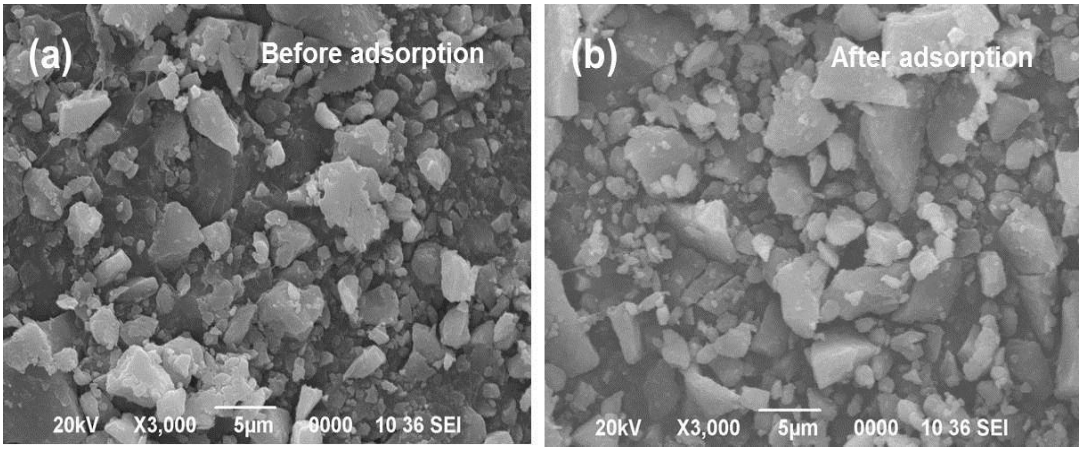

Figure 3A.18. SEM images of LDH3 (a) before and (b) after adsorption of MO.

Figure 3A.19a shows the FTIR spectra of LDH3 after adsorption of MO and inset is enlarged view of the spectra in the wavenumber range of 1000–1300 cm^{-1}. Comparing the spectrum with pure MO and LDH3 (Figure 3A.19b), we have seen that some new peaks arises at 1034, 1123 and 1166 cm^{-1} associated with the vibration of the $–SO_3^-$ group, 1,4-substitutent in the benzene ring and C–N stretching vibration, respectively in MO adsorbed LDH3 [13,51]. Moreover, the adsorption band at 1612 cm^{-1} corresponds to the C=C stretching vibration of the benzene ring of MO which indicates that MO has been well adsorbed on the surface of LDH3. Thus, the enhanced adsorption capacity of LDH3

for removal of MO is associated with the electrostatic attraction between the anionic dye molecule and adsorbent surface. These findings are well supported by the pH study as explained earlier (Figure 3A.8d). The maximum adsorption efficiency for removal of MO is obtained at pH 6 due to the electrostatic attraction between the negatively charged dye molecule and LDH surface. Moreover, the presence of surface hydroxyl groups in the LDH makes it efficient adsorbent by the formation of hydrogen bonding with the sulfonate group of MO dye ($SO^{3-}Na^{+}$), enhancing the absorption capacity of the adsorbent.

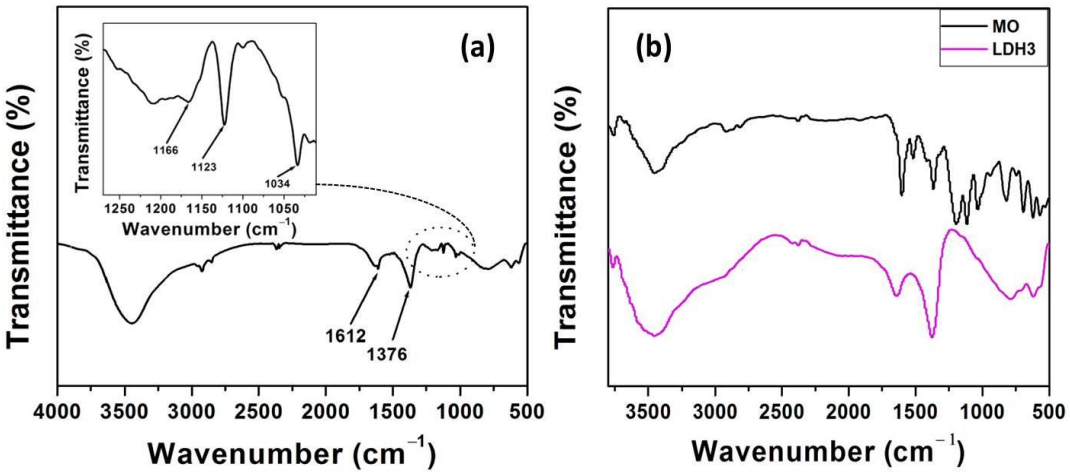

Figure 3A.19. (a) FTIR spectra of LDH3 after adsorption of MO and inset is enlarged view of the spectra in the wavenumber range of 1000–1300 cm^{-1} and (b) FTIR spectra of pure MO and LDH3.

Table 3A.5 shows the comparisons of adsorption of MO onto various adsorbents reported previously in terms of maximum adsorption capacity under various reaction conditions. It is found that LDH3 in the present study is a potential adsorbent for dye removal from aqueous solutions with high value of adsorption capacity under various reaction conditions compared to other adsorbents.

Moreover, a comparative adsorption study was carried out using two more anionic organic dye pollutants such as, congo red (CR) and methyl red (MR) along with methyl orange (MO) over LDH3 under the optimized experimental conditions to utilize the adsorbent for future application. The adsorbent shows efficient adsorption activity for the

anionic dyes, CR and MR with % dye uptake values of 97 and 96%, respectively (Figure 3A.20).

Table 3A.5. Comparison of adsorption of MO onto LDH3 with earlier reports.

Entry	Adsorbents	Surface area of adsorbent (m^2/g)	Dye conc. (mg/L)	Adsorbent amount (mg)	Contact time (min)	Adsorption capacity (mg/g)	Ref.
1	NiMgAl LDH (LDH3)	268	10–70	5	60	127	[This Work]
2	MgNiAl LDH	137.4	10–500	50	40	118.5	[27]
3	Banana peel	20.6–23.5	10–120	100	24 (h)	21	[52]
4	Orange peel	20.6–23.5	10–120	100	24 (h)	20.5	[52]
5	Activated alumina	——	10	100	60	9.8	[53]
6	Modified halloysite nanotubes	47.6	50–200	100	45	91.7	[54]
7	AgNPs-coated AC	——	2–10	——	16 (h)	27.5	[55]

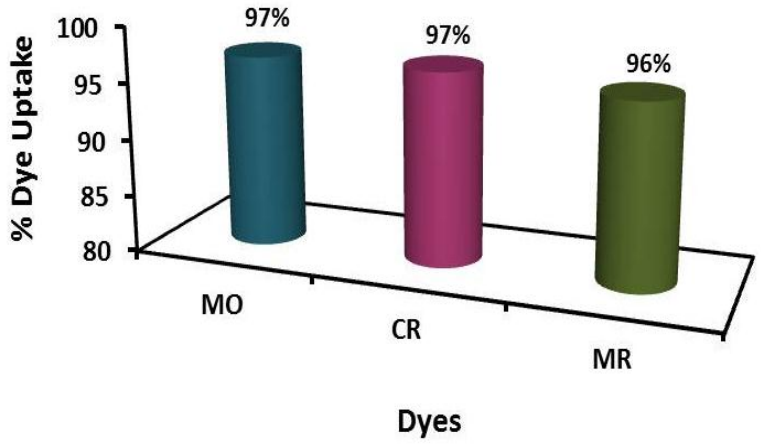

Figure 3A.20. % Dye uptake of various anionic dye pollutants over LDH3 (Optimized conditions: MO concentration = 20 mg/L, adsorbent dose = 5 mg, equilibrium time = 90 min, pH = 6 and *T* = 25 °C).

Reusability of the adsorbent is an important factor in order to establish it as a good adsorbent. For reusability test, desorption study was performed first by subjecting the used adsorbent in Na_2CO_3 solution for 24h. After that, the adsorbent was centrifuged, washed thoroughly with distilled water and dried at 80 °C. The resulting adsorbent was again subjected to multicyclic adsorption process using the same concentration of MO dye and identical adsorbent dosage under same reaction conditions. The regenerated adsorbent shows % dye removal of 95, 91 and 88% for 1st, 2nd and 3rd cycles, respectively indicating potential adsorption capacity of the adsorbent with good reusability (Figure 3A.21).

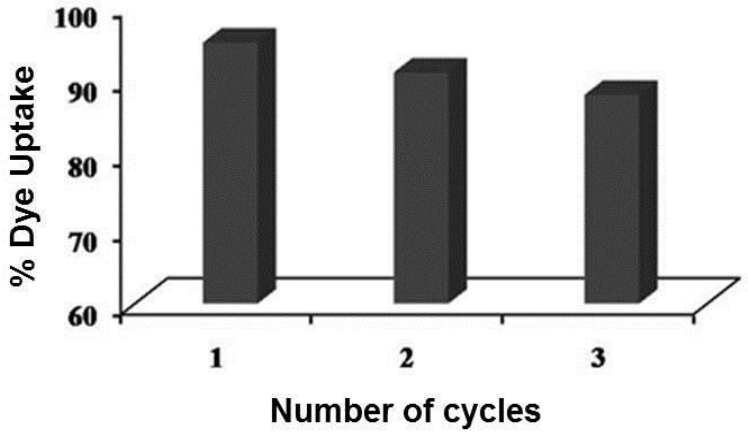

Figure 3A.21. Reusability of LDH3 for adsorption of MO.

In summary, we have demonstrated the study of adsorption of anionic dyes onto various NiMgAl LDHs of variable metal compositions synthesized via co-precipitation method. Introduction of Ni in brucite-like LDH greatly affects the structural as well as the adsorption capacity of the LDH samples. Ternary NiMgAl LDH with Ni/Mg molar ratio of 1:1 (LDH3) possessing high surface area exhibits preferentially higher adsorption capacity for removal of MO from aqueous solution with % dye uptake of 97%. The adsorption process has been influenced by various reaction parameters such as contact time, adsorbent dosages, initial dye concentration and solution pH. The adsorption kinetics study shows that process can be well described with pseudo-second order kinetic model. Langmuir adsorption model displays better fitting with the adsorption data, indicating a monolayer adsorption process. The maximum adsorption capacity, q_m of the LDH3 adsorbent is 127.9 mg/g for MO at optimum pH of 6. The D–R isotherm model

shows that the adsorption process involved is a physical adsorption. Thus, the LDH material could be used as potential adsorbent for removal of anionic dye pollutants from aqueous solution.

Section 3B: Preferential adsorption of various anionic and cationic dyes from aqueous solution over ternary CuMgAl LDH

In this section, we have discussed the preferential adsorption of various anionic and cationic dyes using CuMgAl ternary LDH. The complete characterization of various ternary CuMgAl LDHs with varying molar ratio of Cu/Mg, synthesized via simple co-precipitation route has been discussed thoroughly. The procedures of LDHs synthesis, characterization techniques and adsorption methods are described in Chapter 2.

3B.1 Results and discussion

3B.1.1 Characterization

Table 3B.1 shows the chemical compositions of the LDH samples. The Cu:Mg ratio in the solid samples are considerably same as in the starting solution. The (Cu+Mg):Al molar ratio of the samples have been kept constant at 3 during the synthesis.

The powder XRD patterns of the samples reveal the formation of hydrotalcite (HT)-like LDH with characteristics sharp, intense peak at lower 2θ angles and broad, less intense peaks at higher 2θ angles (Figure 3B.1a). The characteristic peaks are observed at 2θ = 11.6, 23.4, 34.8, 38.8, 46.3, 60.85 and 62.1° corresponding to (003), (006), (012), (015), (018), (110) and (113) crystal planes, respectively for all cases and are consistent with XRD database (JCPDS file no. 41-1428) [56]. It is observed that a decrease in the intensity and sharpness of the (110) and (113) reflections result with increase in Cu content from CuMgAl1 to CuMgAl4 LDH. This is due to the Jahn–Teller distortion occurred with increase in Cu content in the layered structure. However, no other significant change in the position of peaks is observed and this is due to the small difference in the ionic radii of Mg^{2+} (0.72 Å) and Cu^{2+} (0.73 Å). The lattice parameter *a* has been calculated from (110) reflections and the calculated values are 3.04 and 3.06 Å for CuMgAl1 and CuMgAl2 LDH, respectively. But in case of other two (CuMgAl3 and CuMgAl4) LDHs, calculation of the '*a*' value is not possible as the intensity of (110) plane is very low to identify. The lattice parameter '*c*' is also calculated for all the samples

from (003) reflection and are summarized in Table 3B.1. The *c* value gradually increases with increase in Cu content in the LDH framework from CuMgAl1 to CuMgAl4 LDH.

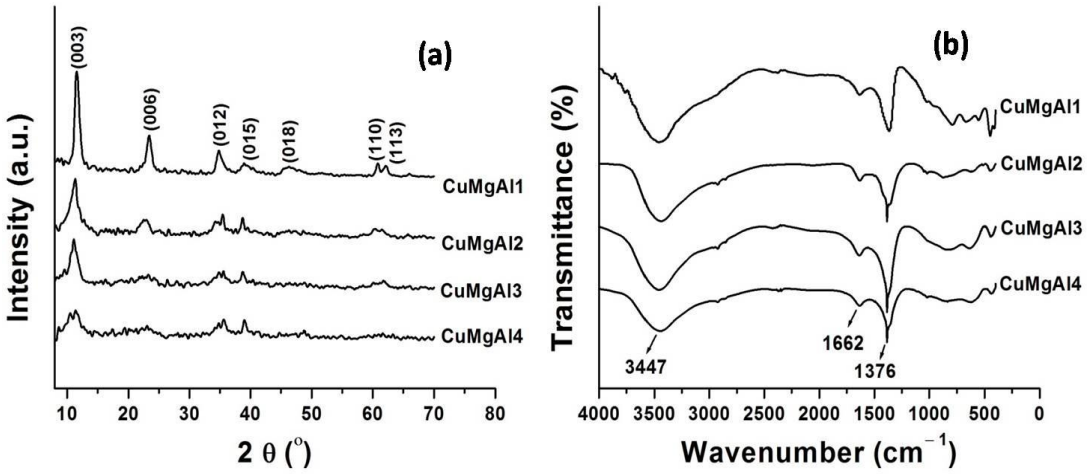

Figure 3B.1. (a) PXRD patterns and (b) FTIR spectra of LDH samples.

FTIR spectra of the LDH samples show stretching vibrations of the typical LDH materials (Figure 3B.1b). The broad adsorption band at around 3447 cm^{-1} is due to the O–H stretching vibration of hydroxyl group present in the layer and the interlayer water molecules. The weak band at around 1662 cm^{-1} is attributed to the −OH bending vibrations of the water molecules. The adsorption band observed at 1376 cm^{-1} is assigned to the asymmetric stretching of carbonate ions. The adsorption bands near 500−800 cm^{-1} are attributed to the stretching vibrations of M−O−H and M−O−M (M = Mg, Cu and Al) bands of LDH.

Table 3B.1. Chemical composition, unit cell parameters and textural properties of various LDH samples.

LDH Samples	**Cu:Mg ratio**		d_{003} **(Å)**	**Unit cell parameter[b] (Å)**	S_{BET} **(m^2/g)**
	Solution	**Solid[a]**		***C***	
CuMgAl1	0:3	0:3.1	7.69	23.07	131
CuMgAl2	1:2	0.9:2.1	7.79	23.37	102
CuMgAl3	1:1	1:1.1	7.97	23.91	89
CuMgAl4	2:1	2.1:1	8.42	25.26	60

[a]Determined by AAS

The thermogram of the samples shows that LDH materials exhibit mainly two weight loss steps (Figure 3B.2a). The first weight–loss step is observed in the temperature range of 50−200 °C and it is attributed to the removal of water molecules physically adsorbed on the layer and in the interlayer region of LDH. The second weight–loss step is due to the brucite layer dehydroxylation as well as the carbonate anions decomposition and is observed in the range of 250−400 °C temperature. Figure 3B.2b shows the Diffuse–reflectance UV-vis spectra of the LDH samples. In all cases, optical absorption band is observed in the range of 200–300 nm and is due to the LMCT (ligand–to–metal charge transfer) in the MO_6 octahedral of the LDHs. The broad band in the visible region of 500–800 nm is due to the MMCT (metal–to–metal charge transfer) M^{II}–O–Al^{III} (M^{II} = Mg or Cu) oxo-bridges linkages in LDHs. The broadness of the band gradually increases with increase in the amount of Cu from CuMgAl2 to CuMgAl4. This is attributed to the ^2E_g (D) → $^2T_{2g}$ (D) transition of Cu^{2+} cation in the distorted octahedral of the LDH framework due to the Jahn-Teller effect. However, the band is not observed in case of CuMgAl1 LDH (without Cu).

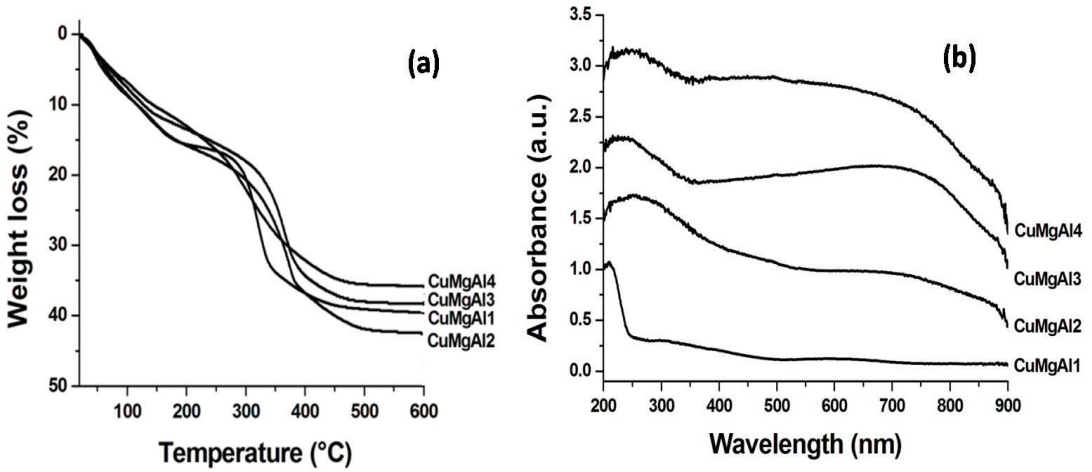

Figure 3B.2. (a) TGA graphs and (b) UV-vis DRS spectra of LDH samples.

Figure 3B.3 shows the SEM images of LDH samples. Flat platelets are observed in case of CuMgAl1 LDH (without Cu). On introduction of Cu into the binary LDH, such platelets are getting overlapped resulting in large irregular particle size (from CuMgAl2 to CuMgAl4 LDH).

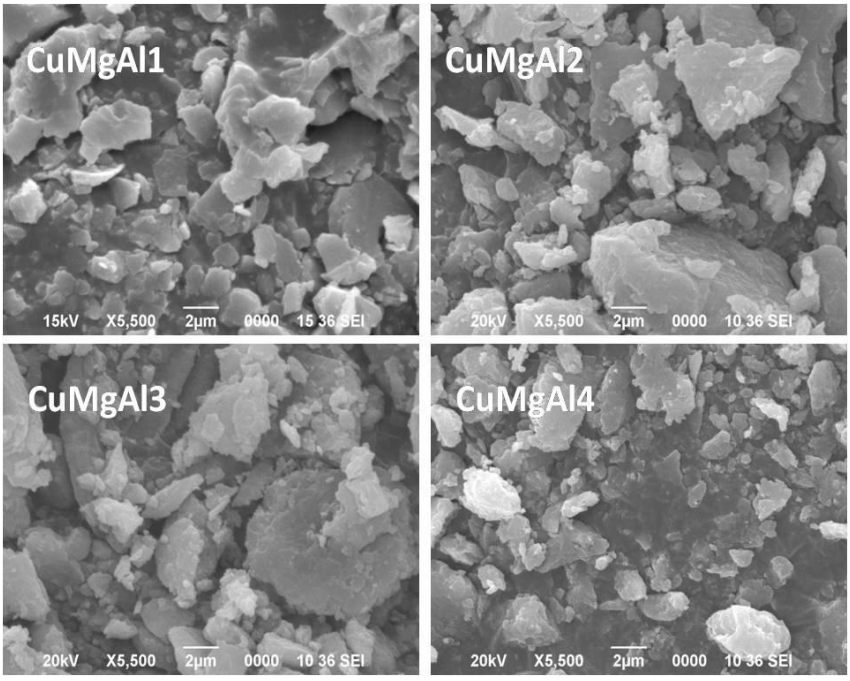

Figure 3B.3. SEM images of LDH samples.

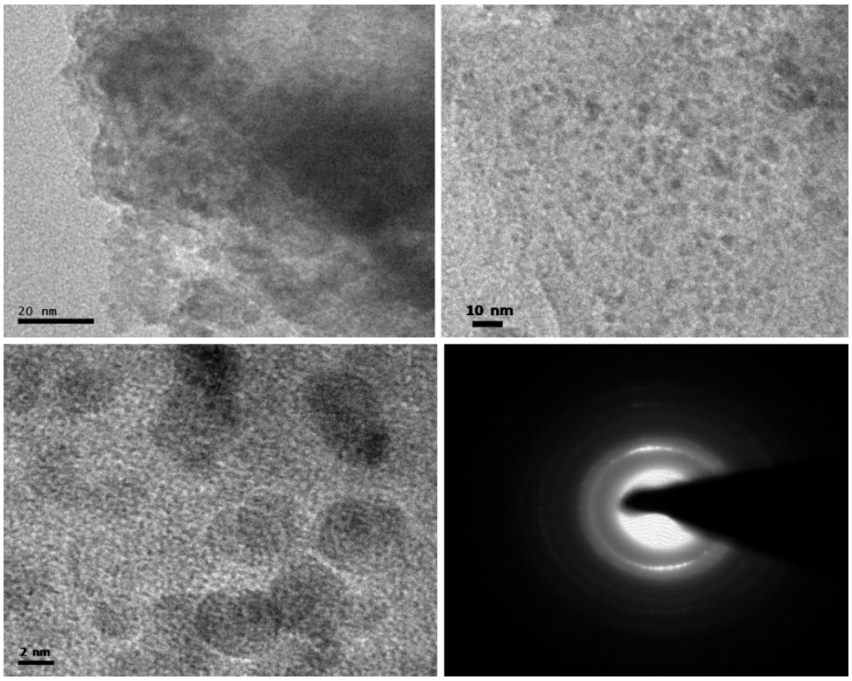

Figure 3B.4. (a–c) TEM images at different resolution and (d) SAED patterns of CuMgAl4 LDH.

TEM analysis of the Cu rich LDH (CuMgAl4 LDH) has been performed and the images at different resolution are shown in Figure 3B.4. It shows that particles are small,

uniform and well dispersed with plate like morphology overlapping on top of another particle. The selected area electron diffraction (SAED) pattern also shows the uniform and crystalline nature of the sample by the formation of different concentric diffraction rings due to different characteristic lattice planes.

The N_2 adsorption–desorption measurements of the LDH samples have been carried out and the isotherms are shown in Figure 3B.5. The N_2 adsorption-desorption isotherms show that all the samples exhibit type II isotherms with small hysteresis loop of type B according to the IUPAC classifications [56]. The closer point of the hysteresis loop is appeared at a relative pressure (P/P_o) of 0.7–0.8 for all the samples, indicating that mesoporous materials exhibit similar pore architecture. The BET surface area values increases with decrease in Cu content in CuMgAl LDH. The calculated BET surface areas are 131, 102, 89 and 60 m^2/g for CuMgAl1, CuMgAl2, CuMgAl3 and CuMgAl4, respectively (Table 3B.1).

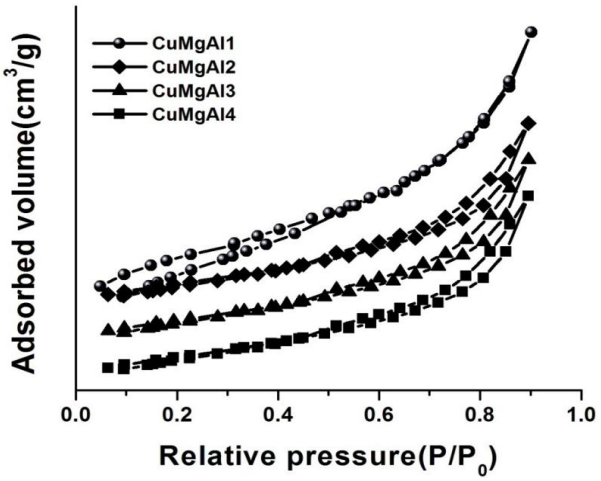

Figure 3B.5. N_2 adsorption-desorption isotherms of LDH samples.

3B.1.2 Adsorption of methyl orange (MO) over various LDH adsorbents

The adsorption experiment was first carried out using methyl orange (MO) as anionic dye. To evaluate the adsorption efficiency of the samples, 5 mg of each of the adsorbents were added to 20 mL of MO solution with concentration of 20 mg/L and allowed to stir for 180 min at room temperature and pH 7. Figure 3B.6 shows the dye removal (%) of MO over various LDHs.

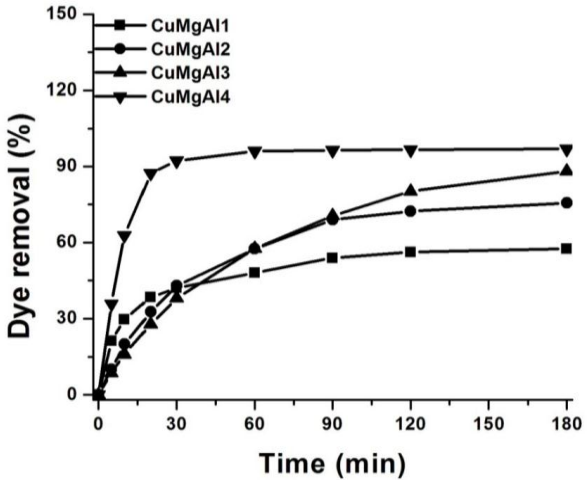

Figure 3B.6. Dye removal (%) of MO over various LDHs ($V_{solution}$ = 20 mL, C_o = 20 mg/L, adsorbent amount = 5 mg, T = 25 °C, pH = 7).

It is seen that the binary CuMgAl1 LDH (without Cu) shows dye removal of 48% and reached an equilibrium state after 90 min. Introduction of Cu into the LDH framework, enhances the adsorption capacity of CuMgAl1 LDH by increasing the dye removal (%) from 48 to 98%. The ternary CuMgAl4 LDH (Cu rich) with Cu:Mg molar ratio of 2:1 shows the highest adsorption capacity for the removal of MO from aqueous solution with % dye removal of 98% and reaches the equilibrium position between 30–60 min. The BET surface area measurements were carried out, but the values are not in accordance with the adsorption efficiency of the adsorbents (Figure 3B.5, Table 3B.1). Therefore, some other factors may be responsible for efficient adsorption of the adsorbents. As the electronegativity increases in the order Mg<Al<Cu, the isomorphous substitution of Mg^{2+} with higher electronegative Cu^{2+} cation prevails the enhanced adsorption of the anionic dyes from aqueous solution by increasing the attractive forces between the positive layers and the anionic dye molecules [57]. Therefore, introduction of higher amount of Cu into the brucite layer provides the strongest adsorption sites by increasing the affinity for anionic dyes in case of CuMgAl4 LDH (Cu rich). Moreover, the possible mechanism for enhanced adsorption efficiency of LDH for removal of anionic dyes from aqueous solution can be understood in terms of (i) electrostatic attraction arises between the negatively charged counter part of dye molecules and the positive LDH surface; and (ii) H-bonding between the surface hydroxyl groups of the LDH and electronegative group of

dye molecules [58,59]. Incorporation of Cu^{2+} into brucite-like layers led to a steep decrease in basicity, but with increasing copper content, surface basicity started to increase, resulting in the increase of the surface hydroxyl groups within the bruicite-like LDH [60]. Hence, increasing amounts of copper favors the adsorption of anionic dye molecules over the surface of Cu-rich LDH (CuMgAl4 LDH) through the formation of H–bonding. Thus, CuMgAl4 LDH has been chosen as the optimum adsorbent over the other adsorbents for further study.

3B.1.3 Preferential adsorption of various anionic and cationic dyes over CuMgAl4 LDH

We have studied the preferential adsorption of various anionic and cationic dyes over CuMgAl4 LDH using 20 mL of each of the dye solution (20 mg/L) and a constant amount of 5 mg adsorbent. The result shows that the anionic dyes preferentially adsorb over the surface of LDH adsorbent in comparison to the cationic dyes (Figure 3B.7).

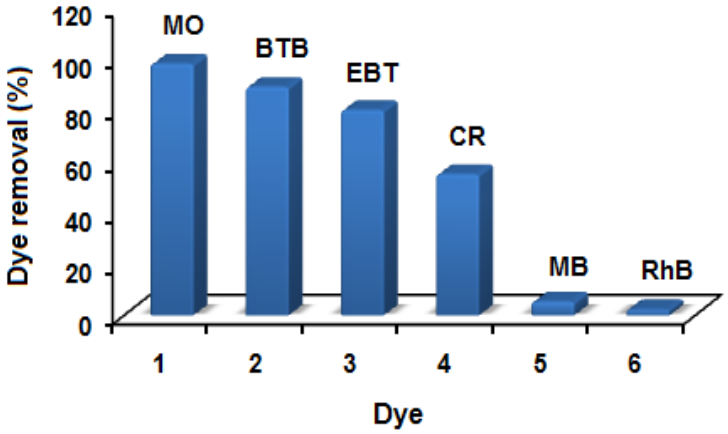

Figure 3B.7. Dye removal (%) of different anionic and cationic dyes over CuMgAl4 LDH ($V_{solution}$ = 20 mL, C_o = 20 mg/L, adsorbent amount = 5 mg, T = 25 °C, pH = 7).

Anionic dyes such as methyl orange, MO (98%); bromothymol blue, BPB (89%); eriochrome black T, EBT (80%); and congo red, CR (55%) are adsorbed in higher amount over CuMgAl4 LDH as compared to the cationic dyes, methylene blue, MB (5%); and rhodamine B, RhB (2%). The positively charged counter parts of the cationic dyes (MB and RhB) resist them from being adsorbed over positively charged LDH surface, resulting

in the lower or negligible dye removal (%). As the results are not significant for cationic dyes, further studies have been carried out using anionic dyes over CuMgAl4 LDH. The corresponding UV-vis spectral changes of the anionic dyes after adsorption over CuMgAl4 LDH are shown in Figure 3B.8.

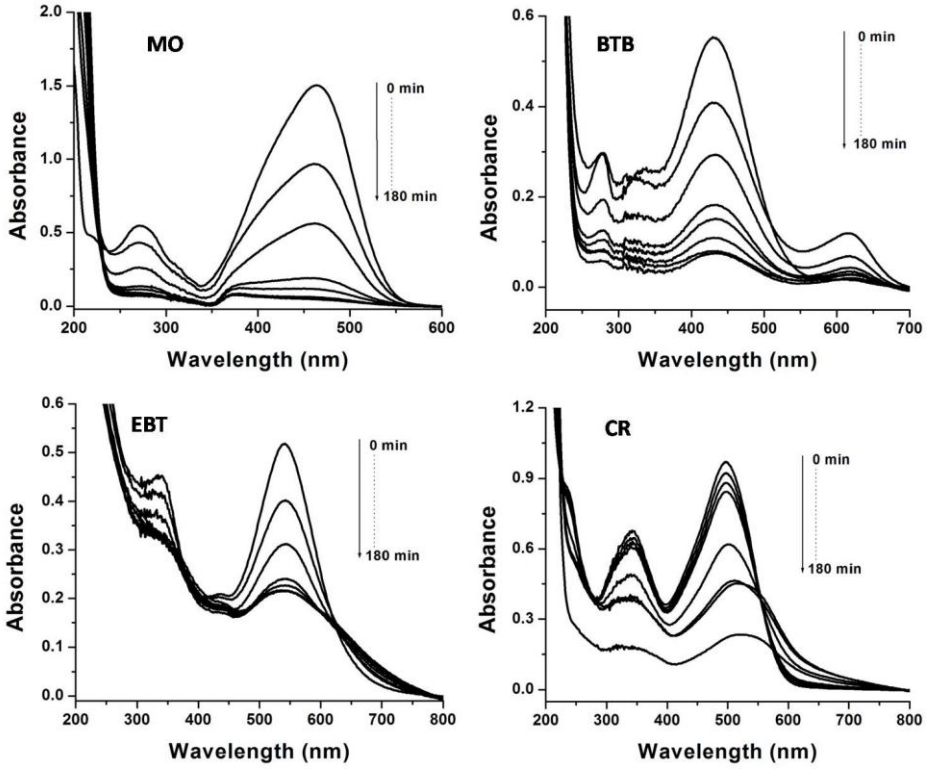

Figure 3B.8. UV-vis spectra of the anionic dyes after adsorption over CuMgAl4 LDH ($V_{solution}$ = 20 mL, C_o = 20 mg/L, adsorbent amount = 5 mg, T = 25 °C, pH = 7).

3B.1.4 Influence of contact time, adsorbent amount, solution pH and dye concentrations

Figure 3B.9a shows the influence of contact time on dye removal (%) of MO, BTB, EBT and CR over CuMgAl4 LDH. The experiment was done using 20 mL of each of the dye solution (20 mg/L) with an adsorbent amount of 5 mg for different contact time (0–180 min). For all dyes, the adsorption sharply increases within first 30 min and then attains a state of equilibrium position within 60 min. The fast adsorption of dyes from aqueous solution within the first 30 min results due to the availability of free active sites on the external surface of the adsorbent.

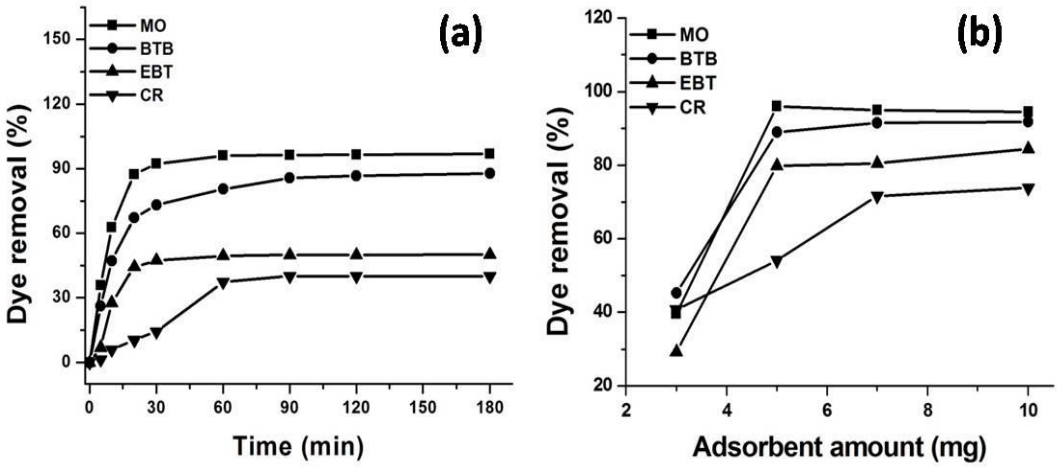

Figure 3B.9. Influence of (a) contact time (min) and (b) adsorbent amount (mg) on dye removal (%) of MO, BTB, EBT and CR over CuMgAl4 LDH ($V_{solution}$ = 20 mL, C_o = 20 mg/L, T = 25 °C, pH = 7).

Figure 3B.9b shows the influence of adsorbent amount on % dye removal of MO, BTB, EBT and CR from aqueous solution. The experiment was performed with initial dye concentration of 20 mg/L with varying adsorbent amount in the ranges of 3–10 mg. For all dyes, it is observed that adsorbent amount has great impact on the adsorption process. With increase in adsorbent amount from 3 to 5 mg, the dye removal (%) of MO also goes on increasing. However, again on increasing the adsorbent amount upto 10 mg, negligible increase in dye removal (%) has been observed and this is because saturation of the adsorbent sites may result at higher adsorbent amount. Similar observations have also been noticed in case of BTB, EBT and CR, but the removal efficiencies are comparatively lower than that of MO. Thus the findings show that 5 mg is the optimum adsorbent amount for all dyes.

Figure 3B.10 shows the influence of solution pH on dye removal (%) of MO, BTB, EBT and CR over CuMgAl4 LDH. The study was carried out with initial dye concentration of 20 mg/L and constant adsorbent amount of 5 mg over the pH ranges of 3–11. The dye removal efficiency is higher at pH 7 with dye removal (%) of 98, 89, 80 and 55% for MO, BTB, EBT and CR, respectively. The enhanced adsorption efficiency of anionic dyes over the LDH surface is ascribed due to the electrostatic attraction between the positive surface sites of the adsorbent and anionic dye molecules. At pH 5, decreases

in the dye efficiency have been observed with removal (%) of 69, 63, 46 and 39% for MO, BTB, EBT and CR, respectively.

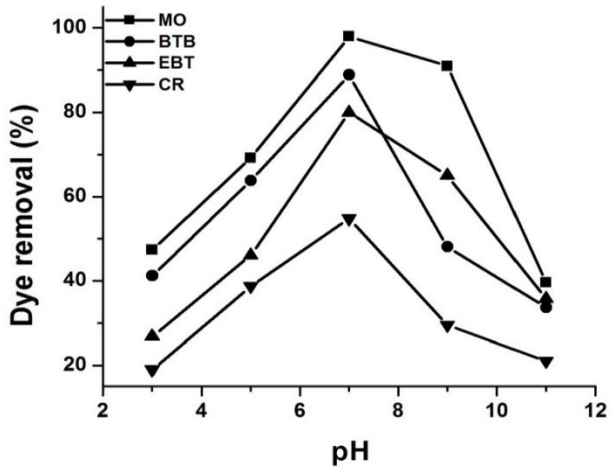

Figure 3B.10. Influence of pH on dye removal (%) of MO, BTB, EBT and CR over CuMgAl4 LDH ($V_{solution}$ = 20 mL, C_o = 20 mg/L, adsorbent amount = 5 mg, T = 25 °C).

Again on decreasing the pH to 3, the dye removal (%) is decreased to 47, 41, 27 and 19% for MO, BTB, EBT and CR, respectively. Dissolution of the adsorbent materials takes place at lower pH solution which results in the unavailability of the active adsorbent sites in the LDH surfaces, thereby resulting in the decrease of dye removal efficiency at pH<7. Similarly, on increasing the solution pH to 9, decrease in removal efficiency (91, 48, 65 and 30% for MO, BTB, EBT and CR respectively) has been observed. Further increasing the solution pH to 11, the dye removal (%) is again deceased to 40, 34, 36 and 21% for MO, BTB, EBT and CR, respectively. This decrease in the adsorption efficiency at higher pH can be explained on the basis of electrostatic repulsion. At higher pH (pH>7), the adsorbent surfaces become highly negatively charged causing an electrostatic repulsion between the anionic organic dye molecules and the negative adsorbent surface sites, which prevent the dye molecules to adsorbed over the adsorbent surface [5].

The influence of initial dye concentrations on adsorption process was studied with a series of dye solutions of various concentrations (10–70 mg/L) using 5 mg of the adsorbent and results are shown in Figure 3B.11.

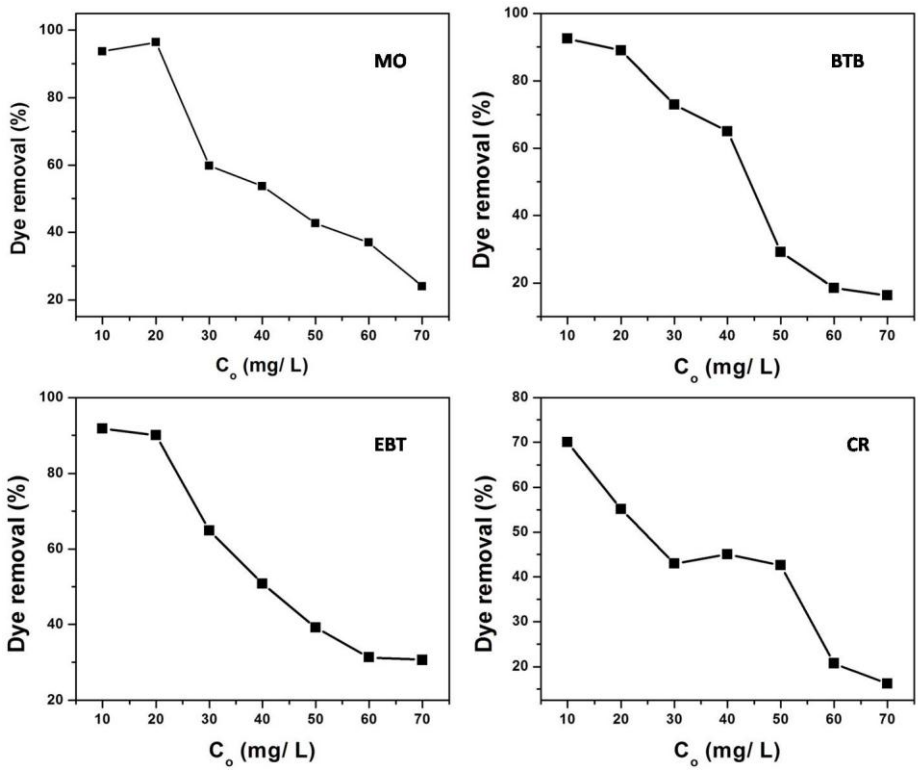

Figure 3B.11. Influence of initial dye concentrations on dye removal (%) of MO, BTB, EBT and CR over CuMgAl LDH ($V_{solution}$ = 20 mL, adsorbent amount = 5 mg, T = 25 °C, pH = 7).

It is seen that the % dye removal gradually decreases with increase in dye concentrations from 10 to 70 mg/L in all the cases. For MO, dye removal (%) decreases from 98 to 24%. Similarly, for BTB, EBT and CR, the decrease in dye removal (%) occurs from 93 to 16%, 92 to 31% and 70 to 16%, respectively. At higher dye concentration, the ratio of available adsorbent surface sites to the initial mole numbers of dye is high; as a consequence the fractional adsorption is dependent on the initial dye concentration [27]. Adsorption of a certain fixed amount of dye concentration over the adsorbent surface results in the unavailability of the free adsorptive sites and thereby results in the decrease of dye removal (%) with increase in initial concentration of dye for the all cases. Adsorption of a certain fixed amount of dye concentration over the adsorbent surface results in the unavailability of the free adsorptive sites due to which decrease in the dye removal (%) took placed with increase in initial dye concentration.

3B.1.5 Adsorption kinetics

The adsorption kinetics was evaluated with pseudo-first and second order kinetic models for understanding the characteristics of the adsorption process using equations 2.6 and 2.7, respectively. Figure 3B.12 shows the pseudo-first order kinetic plots for adsorption of MO, BTB, EBT and CR over CuMgAl4 LDH. Various kinetic parameters have been calculated from the linear plots of log (q_e–q_t) versus t and are summarized in the Table 3B.2. The correlation coefficient value, R^2 for MO, BTB, EBT and CR are 0.906, 0.965, 0.885 and 0.981, respectively.

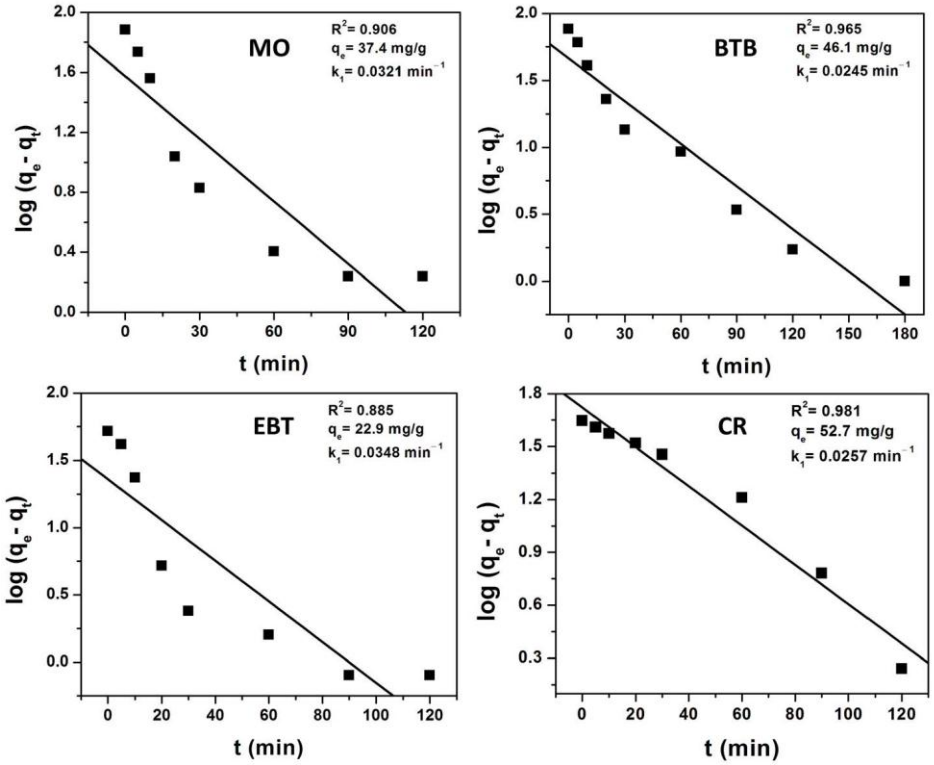

Figure 3B.12. Pseudo-first order kinetic plots for adsorption of MO, BTB, EBT and CR over CuMgAl4 LDH ($V_{solution}$ = 20 mL, C_o = 20 mg/L, adsorbent amount = 5 mg, T = 25 °C, pH = 7).

Figure 3B.13 shows the pseudo-second order kinetic plots for adsorption of MO, BTB, EBT and CR over CuMgAl4 LDH. The kinetic parameters have been obtained from the linear plots of t/q_t versus t and are summarized in the Table 3B.2. The observed correlation coefficient (R^2) values are 0.998, 0.996, 0.995 and 0.985 for MO, BTB, EBT

and CR, respectively. Thus, for all the dyes, it is seen that the adsorption process is better described with a pseudo-second order kinetic model in terms of higher correlation coefficient value (R^2) than that of first order kinetic model.

Table 3B.2. Pseudo-first order and second order kinetic parameters for adsorption of different dyes over CuMgAl4 LDH.

Dye	Pseudo-first order			Pseudo-second order		
	q_e (mg/g)	k_1 (min^{-1})	R^2	q_e (mg/g)	k_2 (g/mg·min)	R^2
MO	37.4	0.0321	0.906	79.2	0.0021	0.998
BTB	46.1	0.0245	0.965	81.1	0.0012	0.996
EBT	22.9	0.0348	0.885	54.8	0.0023	0.995
CR	52.7	0.0257	0.981	74.6	0.0001	0.985

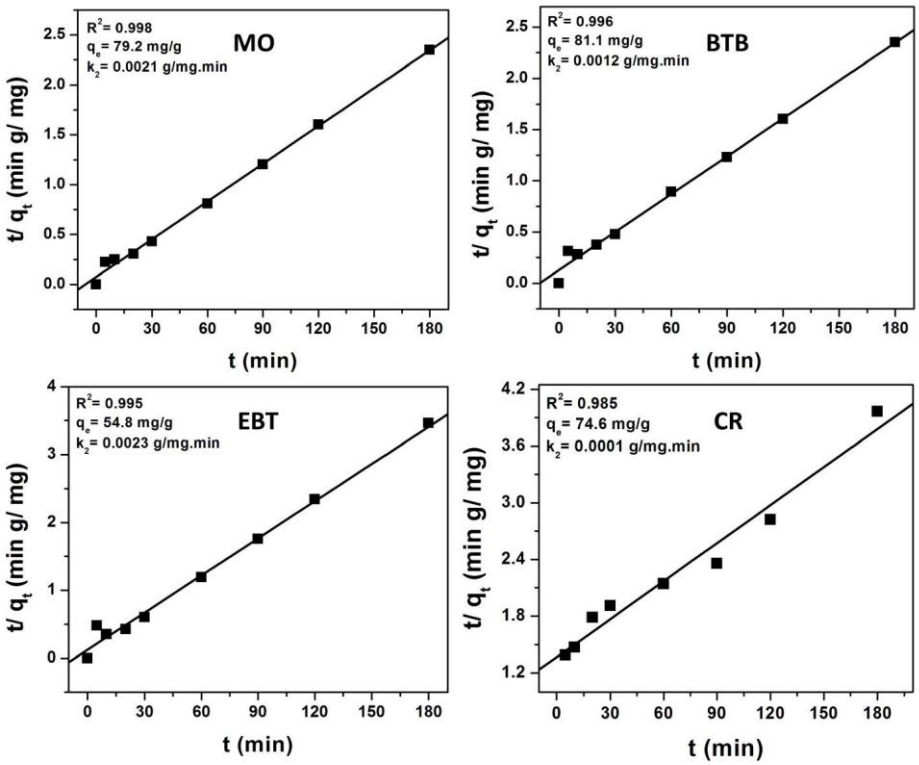

Figure 3B.13. Pseudo-second order kinetic plots for adsorption of MO, BTB, EBT and CR over CuMgAl4 LDH ($V_{solution}$ = 20 mL, C_o = 20 mg/L, adsorbent amount = 5 mg, T = 25 °C, pH = 7).

The diffusion mechanism of the adsorption process was investigated by the intraparticle diffusion kinetic model using equation 2.8. Various kinetic parameters have been calculated from the slope and intercept of the plots of q_t versus $t^{1/2}$ (Figure 3B.14). For all cases, it is observed that the adsorption process is affected by more than one process. Besides the intraparticle diffusion mechanism, some other kinetic mechanism may play important role simultaneously [5]. The plots are linear and do not passes through the origin. The first portion of the plot indicates the adsorption on the external surface and the second portion indicates adsorption through pores of the adsorbent (intraparticle diffusion). The third portion of the plot indicates the unavailability of the free adsorptive sites reaching the equilibrium stage [11].

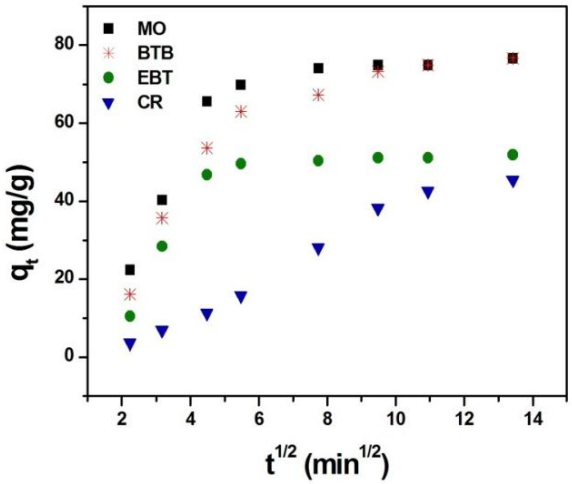

Figure 3B.14. Intraparticle diffusion kinetic plot for adsorption of MO, BTB, EBT and CR over CuMgAl4 LDH ($V_{solution}$ = 20 mL, C_o = 20 mg/L, adsorbent amount = 5 mg, T = 25 °C, pH = 7).

3B.1.6 Adsorption isotherm

The adsorption capacity of the adsorbent at different equilibrium concentrations was studied using Langmuir and Freundlich isotherm models using equations 2.9 and 2.11, respectively. The isotherm study also provides information about the distribution of the adsorbates between solid and liquid phase on reaching the equilibrium state of adsorption. Figure 3B.15 shows the Langmuir isotherm plots for adsorption of MO, BTB, EBT and CR over CuMgAl4 LDH.

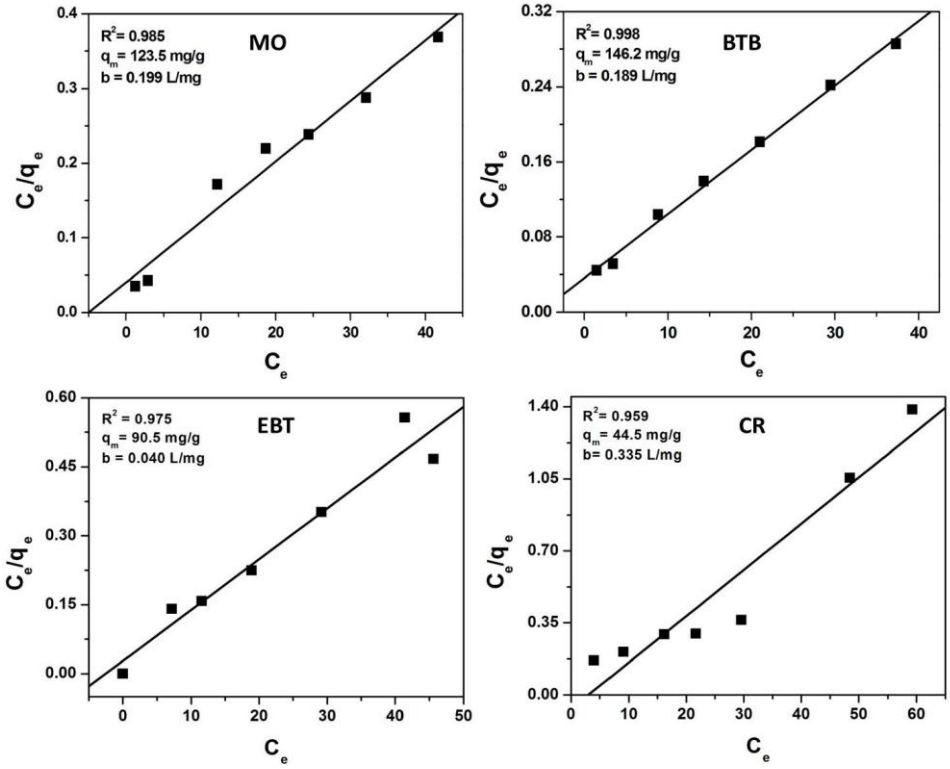

Figure 3B.15. Langmuir isotherm plots for adsorption of MO, BTB, EBT and CR over CuMgAl4 LDH ($V_{solution}$ = 20 mL, adsorbent amount = 5 mg, T = 25 °C, pH = 7).

Various isotherm parameters have been calculated from the linear plot of C_e/q_e versus C_e and are summarized in Table 3B.3. The adsorption data shows best fitting with the Langmuir isotherm model with relatively higher correlation coefficient (R^2) values for all the cases. The calculated R^2 values are 0.985, 0.998, 0.975 and 0.959 for MO, BTB, EBT and CR, respectively. The maximum adsorption capacity, q_m calculated from the isotherm are 123.5, 146.2, 90.5 and 44.5 mg/g for MO, BTB, EBT and CR, respectively. The isotherm also provides information on the favorability of the adsorption process from the value of dimensionless constant separation factor or equilibrium parameter (R_L) which is given by equation 2.10. The calculated R_L values are between 0 and 1 for all the cases, indicating favorable adsorption of MO, BTB, EBT and CR over CuMgAl4 LDH (Table 3B.3).

Table 3B.3. Langmuir, Freundlich and Dubinin–Radushkevich (D–R) isotherm parameters for adsorption of different dyes over CuMgAl4 LDH.

Dye	Langmuir model				Freundlich model			D–R model			
	R^2	q_m mg/g	b L/mg	R_L	R^2	k_F (mg/g) $(L/mg)^{1/n}$	n	R^2	q_o mg/g	k_{DR} mol^2/kJ^2	E kJ/mol
MO	0.985	123.5	0.199	0.2	0.942	38.5	3	0.921	94.9	0.469	1.03
BTB	0.998	146.2	0.189	0.2	0.971	34.5	3	0.950	109.2	0.763	8.09
EBT	0.975	90.5	0.040	0.6	0.923	39.3	5	0.799	77.1	0.337	1.22
CR	0.959	44.5	0.335	0.1	0.542	24.6	4	0.845	60.6	3.19	0.396

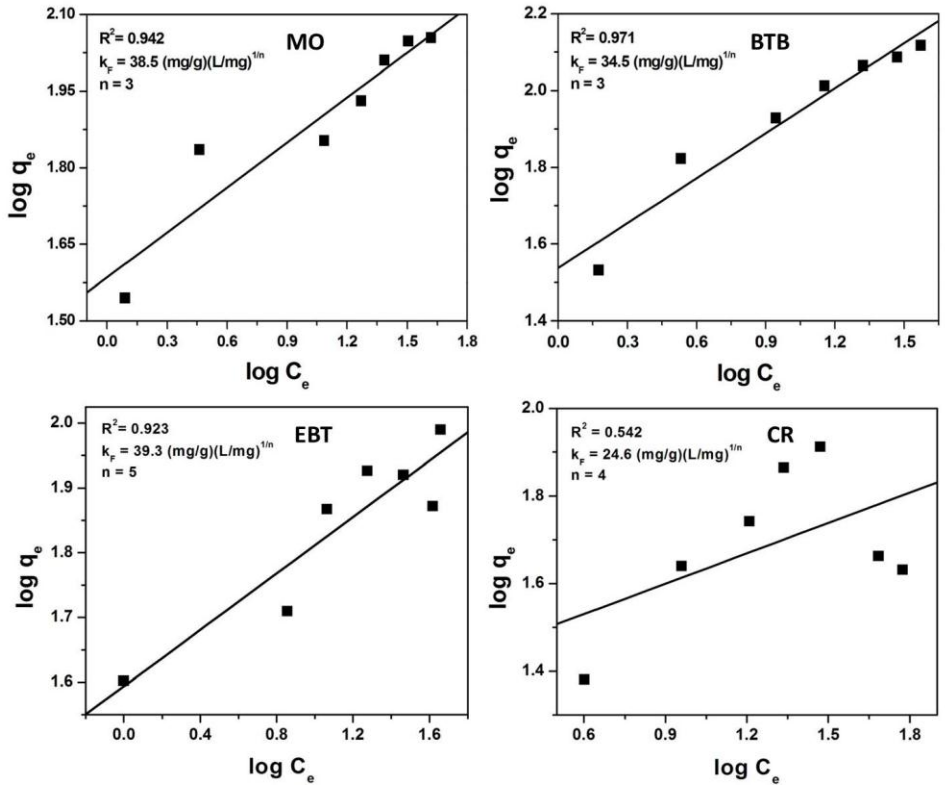

Figure 3B.16. Freundlich isotherm plots for adsorption of MO, BTB, EBT and CR over CuMgAl4 LDH ($V_{solution}$ = 20 mL, adsorbent amount = 5 mg, T = 25 °C, pH = 7).

Figure 3B.16 shows the Freundlich isotherm plots for adsorption of MO, BTB, EBT and CR over CuMgAl4 LDH. The values of various isotherm parameters have been

calculated from the linear plot of log q_e versus log C_e and are summarized in Table 3B.3. It is observed that the correlation coefficient (R^2) values are comparatively less than that of Langmuir isotherm model for all the dyes. The calculated n values are in the range of 1–10 for all the cases indicating favourable adsorption of MO, BTB, EBT and CR over CuMgAl4 LDH.

The adsorption isotherm was also analyzed with Dubinin–Radshkevich (D–R) isotherm model using equation 2.12 and plots are displayed in Figure A.1 of Appendix. Various isotherm parameters have been calculated from the linear plot and are summarized in Table 3B.3. The mean adsorption energies (E) for all the dyes have been calculated using the equation 2.14. The E values between 1–16 kJ/mol imply that the adsorption process is a physical phenomenon while the values more than 16 kJ/mol imply chemisorption process [51]. In this study, the obtained E values are in the range of 0.3961–8.09 kJ/mol for all the dyes (Table 3B.3), indicating physical nature of the adsorption process.

To gain insights into the adsorption mechanism, FTIR analysis of the CuMgAl4 LDH, pure and adsorbed MO, BTB, EBT and CR have been carried out and are shown in Figure 3B.17. In case of MO adsorbed LDH, appearance of some new bands in the range of 1000–1300 cm^{-1} indicate that MO has been well adsorbed on the surface of CuMgAl4 LDH. The bands at 1021 and 1118 cm^{-1} correspond to the vibration of the $–SO_3^-$ group and 1, 4-substitutent of the benzene ring of MO dye, respectively [13,52]. The band at 1177 cm^{-1} is due to the C–N stretching vibration of MO and the band around 1609 cm^{-1} corresponds to C=C stretching vibration of the MO benzene ring. Similarly, for BTB, EBT and CR, appearance of some new bands in the range of 1000–1300 cm^{-1} confirms their presence in the LDH structure. These new bands assigned to $–SO_3^-$ group in all the three cases and C–N stretching vibration in CR and EBT.

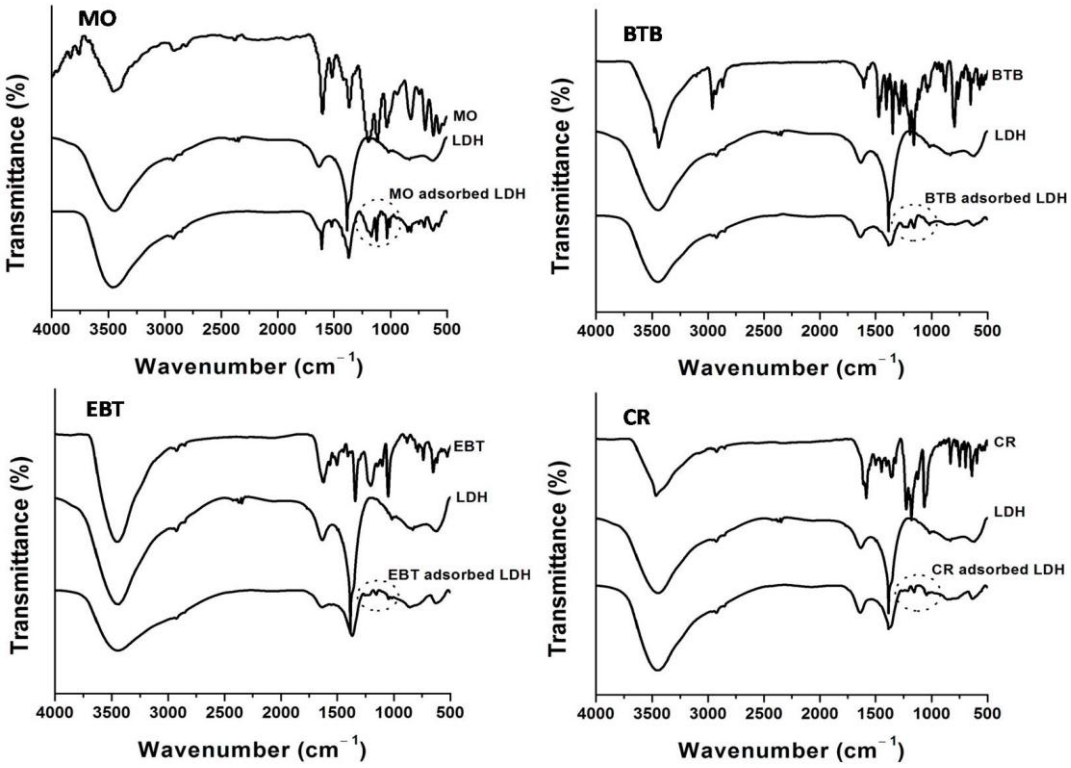

Figure 3B.17. FTIR spectra for adsorption of MO, BTB, EBT and CR over CuMgAl4 LDH.

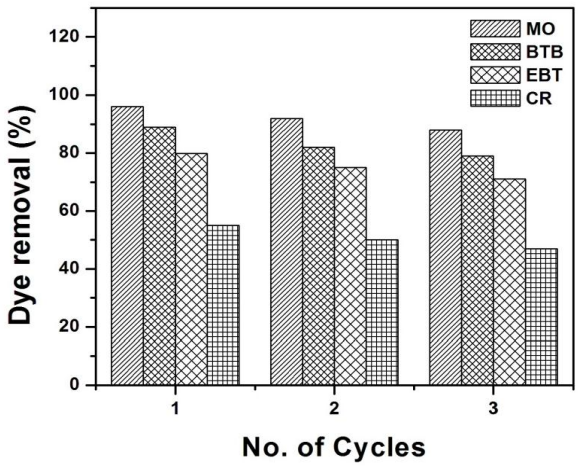

Figure 3B.18. Multicyclic adsorption of MO, BTB, EBT and CR over CuMgAl4 LDH ($V_{solution}$ = 20 mL, C_o = 20 mg/L, adsorbent amount = 5 mg, T = 25 °C, pH = 7).

Multicyclic adsorption study of CuMgAl4 LDH was carried out for each case and the results are shown in Figure 3B.18. Desorption study was first performed before the recyclability test by suspending the used adsorbent in the solution of Na_2CO_3 and stirred

for 24h. The adsorbent was then separated by centrifuging, washed thoroughly with distilled water and dried overnight at 80 °C. After the recovery, the adsorbent was again subjected to multicyclic adsorption for all dyes under same reaction conditions. The recovered adsorbent shows dye removal efficiencies of 98, 92 and 88% for MO in the three respective cycles. For BTB, the removal efficiencies are 89, 82 and 79% for 1st, 2nd and 3rd cycle, respectively. Again, for EBT, the dye removal efficiencies are 80, 75 and 71%, while the efficiencies are 55, 50 and 47% for CR in the respective three cycles.

3B.1.7 Selective adsorption of dye from a mixture of anionic and cationic dyes

The selective adsorption study with a mixture of anionic and cationic dyes have been carried out by pH variation over CuMgAl4 LDH and are shown in Figure 3B.19.

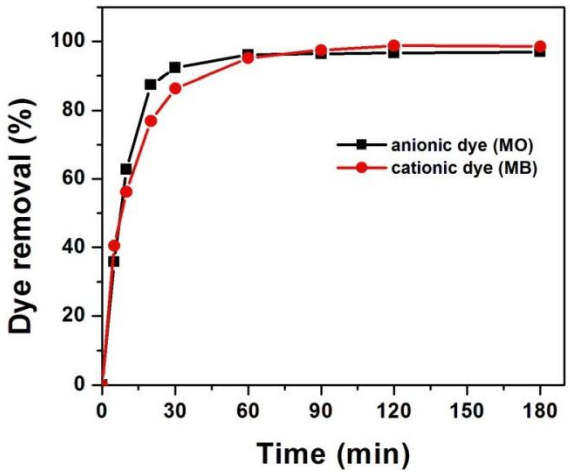

Figure 3B.19. Selective adsorption of dye from a mixture of anionic and cationic dyes over CuMgAl4 LDH ($V_{solution}$ = 20 mL, C_o = 20 mg/L, adsorbent amount = 5 mg, T = 25 °C, pH = 7 for MO and 11 for MB).

Here, we have used methyl orange (MO) and methylene blue (MB) as anionic and cationic dye, respectively. The removal of the respective dyes from the mixture depends upon the solution pH. CuMgAl4 LDH can efficiently remove anionic dye, MO from the mixture of anionic and cationic dyes at pH 7 with dye removal (%) of 98%. This is due to the electrostatic attraction between the positive surface site of LDH adsorbent and negative counterpart ($R–SO_3^-$) of anionic MO dye. Again, for cationic MB dye in the dye mixture, LDH shows efficient adsorption activity with dye removal (%) of 98.5% at higher pH (pH

= 11). This is because at higher pH, LDH surface acquire highly negative charges, resulting in the electrostatic interaction with the positive counterpart ($R–S^+$) of cationic MB dye. Thus, CuMgAl4 LDH can selectively remove dye from a mixture of anionic and cationic dyes.

In summary, a comparative study was employed for adsorption of various anionic and cationic dyes over ternary CuMgAl LDH. A co-precipitation method has been used to synthesize the LDH samples with varying compositions of Cu and Mg. The activity measurements of the synthesized materials have been tested for adsorptive removal of various anionic and cationic dyes from aqueous solution. The Cu-rich LDH, CuMgAl4 LDH with Cu/Mg 2:1 shows efficient adsorption activity for removal of organic dye pollutant. Moreover, a comparative study shows that the anionic dyes such as methyl orange (MO), bromothymol blue (BTB), eriochrome black T (EBT) and congo red (CR) efficiently adsorbed over the LDH surface compared to the cationic dyes, methylene blue (MB) and rhodamine B (RhB) at pH 7. The electrostatic attraction between the positive surface sites of LDH adsorbent and anionic counter parts of the respective dye molecules are mainly responsible for the preferable adsorption of anionic dyes over the LDH surface. The adsorption process follows a pseudo-second order kinetic model. Langmuir isotherm model shows best fitting to the isotherm data compared to Freundlich isotherm model in terms of higher correlation coefficient value indicating a monolayer adsorption of MO, BTB, EBT and CR over LDH surface. A physisorption process is found to involve in the adsorption of anionic dyes over the LDH surface. The adsorbent could be reused for multicyclic adsorption process with significant adsorption efficiency.

Section 3C: Adsorptive removal of congo red from aqueous solution by sonochemically synthesized NiAl layered double hydroxide

In this section, we have demonstrated the synthesis of NiAl LDHs via co-precipitation method followed by ultrasonic irradiation and tested as adsorbents for removal of congo red (CR) dye from aqueous solution. During the synthesis, the material was subjected to various ultrasonic irradiation times to see the effect of irradiation time on structural as well as on the adsorption property of the materials. The complete characterizations of the synthesized LDHs have been described herein. The synthesis procedures of LDHs, detailed characterization techniques and adsorption methods were discussed in Chapter 2.

3C.1 Results and discussion

3C.1.1 Characterization of the adsorbents

The powder XRD patterns of the samples are displayed in Figure 3C.1. The formation of typical hydrotalcite (HT)-type LDH materials can be revealed from the figure which exhibit the characteristic sharp and highly intense peaks at lower side of the 2θ angles; and broad and very less intense peaks at higher side of 2θ angles [14,61]. The diffraction peaks approximately at 2θ = 11.6, 23.4, 34.8, 60.85 and 62.1° are indexed as (003), (006), (012), (110) and (113) reflections, respectively. The d-spacing and unit cell parameters of the adsorbents have been calculated and presented in Table 3C.1. The value of cell parameters '*a*' and '*c*' can be obtained from (110) and (003) reflections as $a = 2d_{110}$ and $c = 3d_{003}$, respectively. The unit cell parameter '*a*' characterizes the average metal-metal distances within the brucite layers [42]. The cell parameter '*c*' is associated with the thickness of the interlayer governed by the average metal cation charge, nature of the anions in the interlayer region and water molecules present [14,42]. All the adsorbents exhibit similar values of cell parameter '*a*'. The *c* value is higher for sonochemically synthesized NiAl LDH (NiAl-S_1 LDH) than synthesized under normal reflux condition (NiAl-R) (Table 3C.1). However, ultrasonic irradiation time doesn't affect so much on the *c* parameter. For NiAl LDH synthesized under 0.5h (NiAl-$S_{0.5}$ LDH) and 2h (NiAl-S_2 LDH) ultrasonic irradiation time, *c* values are even lower than NiAl-R. The average

crystallite size for (003) and (110) reflections has been calculated for all the adsorbents and presented in Table 3C.1. The crystallite sizes of sonochemically synthesized LDHs are lower compared to the LDH synthesized under normal reflux condition. This is because on exposure to ultrasound waves, cavitation is created within the materials in which bubbles are formed and collapsed. This results in the creation of unique hot spots achieving high pressures, temperatures and excess heating and cooling rates resulting in the formation of materials with smaller crystallite sizes [14,62]. However, the crystallite sizes for NiAl-S_1 LDH is higher compared to the other two sonochemically synthesized LDHs.

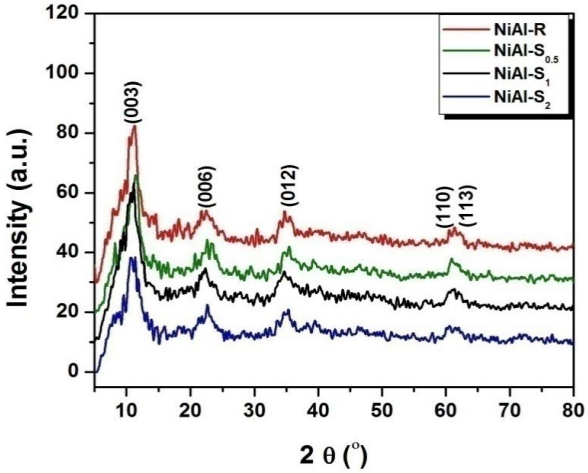

Figure 3C.1. Powder X-ray diffraction patterns of all the samples.

Table 3C.1. Unit cell parameters and average crystallite sizes of all the samples.

Samples	d_{003} (Å)	d_{110} (Å)	Unit cell parameters[a] (Å)		Crystallite size[b] (Å)	
			c	*a*	(003)	(110)
NiAl-R LDH	7.87	1.51	23.61	3.02	27.2	37.8
NiAl-$S_{0.5}$ LDH	7.73	1.51	23.19	3.02	23.8	36.5
NiAl-S_1 LDH	7.94	1.51	23.82	3.02	24.8	36.7
NiAl-S_2 LDH	7.81	1.51	23.39	3.02	23.3	35.0

[a] $a = 2d_{110}$, $c = 3d_{003}$. [b] Calculated using Debye-Scherer formula.

FTIR spectra of the LDH samples show stretching vibrations of the typical LDH materials (Figure 3C.2a). The broad peak around 3439.5 cm^{-1} is corresponding to the stretching vibration of –OH group of the LDH layers and the water molecules present within the interlayer region [5]. The weak peak observed around 1638.2 cm^{-1} is associated with the −OH bending vibrations of water molecules [5]. The FTIR peak observed around 1393.3 cm^{-1} can be assigned as the asymmetric stretching vibration of carbonate ions [63]. The bands observed below 1000 cm^{-1} (near 500−800 cm^{-1}) is associated with the stretching vibrations of metal−oxygen−metal and metal−oxygen−hydrogen bands (metal = Ni and Al) [42]. Figure 3C.2b shows the TGA plots of the LDH samples. Two major weight loss steps can be observed for LDH materials with first weight–loss between 50–200 °C and second loss in the temperature range of 250–400 °C. The first weight–loss is associated with the dehydration of water molecules physically adsorbed on LDH surface. The second loss is associated with the dehydroxylation and decomposition of the carbonate anions within interlayer region [64].

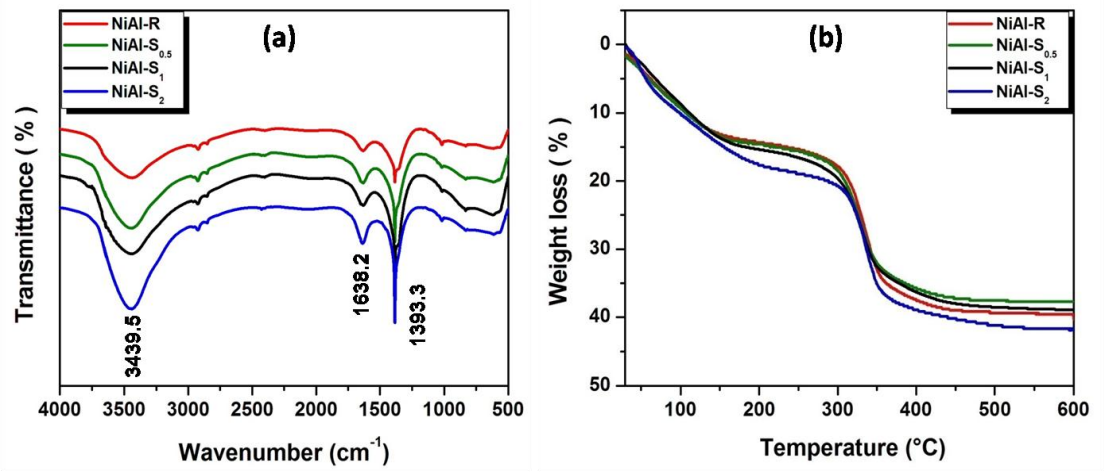

Figure 3C.2. (a) FTIR spectra and (b) TGA curves of all the samples.

Figure 3C.3a displays the SEM image of NiAl-S_1 LDH. It can be observed that small plate-like shapes of the LDH material get agglomerated resulting in the crystallites of large irregular particle size. Similar results can be observed in case of other LDH materials also (Figure A.2 of Appendix). Overlapping of the particles with plate-like shapes of NiAl-S_1 LDH is clearly observed from the TEM image (Figure 3C.3b). The lattice fringes of NiAl-S_1 LDH is displayed in Figure 3C.3c and it is indexed as the (003)

plane with *d* spacing of 0.78 nm. Figure 3C.3d shows the selected area electron diffraction (SAED) patterns of NiAl-S_1 LDH. Appearance of different concentric diffraction rings reveals the formation of uniform, well crystalline LDH materials with plate-like morphology.

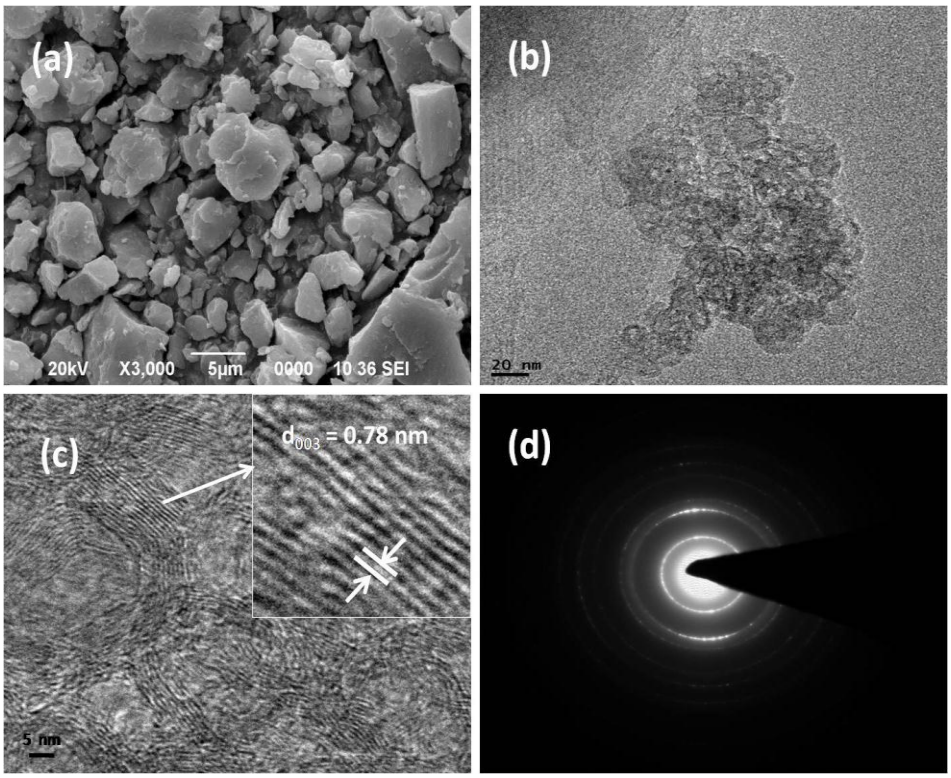

Figure 3C.3. (a) SEM image, (b) TEM image, (c) lattice fringes of (003) plane and (d) SAED pattern of NiAl-S_1 LDH.

3C.1.2 Adsorption experiments

The adsorption experiments were employed to study the adsorption efficiency of the sonochemically synthesized NiAl LDHs under different ultrasonic irradiation time towards the removal of CR and results are presented in Figure 3C.4. The study was done using 10 mg/L of the dye solution (20 mL) with 10 mg of the adsorbents at 25 °C and pH 6. NiAl-S_1 LDH significantly removes almost 96.1% of CR within a very short period of time (30 min). The other two LDHs synthesized under 0.5 and 2h ultrasonic irradiation time (NiAl-$S_{0.5}$ and NiAl-S_2 LDH) remove 85.5 and 85.3% of CR and require 90 min to reach the equilibrium position. The effect of the synthetic method has also been studied by

comparing the dye removal efficiencies of NiAl LDH synthesized under ultrasound irradiation (NiAl-S_1 LDH) and normal reflux method (NiAl-R LDH). The dye removal (%) is higher for NiAl-S_1 LDH (96.1%) than NiAl-R LDH (83.4%). The adsorption equilibrium time is also shorter for NiAl-S_1 LDH (30 min) than NiAl-R LDH. During the synthesis, application of ultrasound wave increases the liquid mixture movement resulting in the formation of bubbles which are capable of controlling the temperature and pressure within the reaction medium in order to achieve rapidity in the reaction time [14,65]. Also ultrasound irradiation time of 1h is the optimum time to produce sufficient microbubbles required for controlling the particle size and surface area. The N_2 adsorption-desorption measurement for NiAl-S_1 LDH was carried out as surface area is one of the essential factors for an efficient adsorbent. The measurement shows the BET surface area value of 29 m^2/g, along with the pore diameter and volume of 3.194 nm and 0.008 cm^3/g, respectively. Thus, NiAl-S_1 LDH shows preferable adsorption capacity for CR and we have selected it as the best adsorbent over the other adsorbents for our further study.

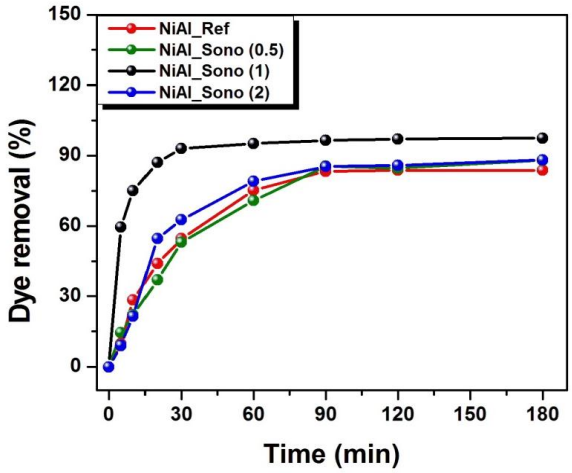

Figure 3C.4. Dye removal (%) of CR on various LDHs with time (10 mg/L CR, 10 mg adsorbent, T = 25 °C).

3C.1.3 Effect of contact time, adsorbent amount, initial dye concentration and solution pH on adsorption of CR

The corresponding UV-vis spectral change for adsorption of CR on NiAl-S1 LDH is depicted in Figure 3C.5a. The maximum absorption peak of CR (λ_{max} = 497 nm) gradually

diminishes with time and attain an equilibrium position after a particular time (equilibrium time). The effect of contact time on adsorption process towards the removal of CR was determined with 20 mL of the CR solutions and 10 mg of NiAl-S_1 LDH for 180 min and is shown in Figure 3C.5b. Here, we have used two different concentrations of CR solution (10 and 30 mg/L). For both the cases, it is observed that the adsorption of CR on NiAl-S_1 LDH increases considerably upto a particular time. A sharp increase in the adsorption rate is observed within the first 30 min, and after that it goes slow and reaches an equilibrium position within 30–60 min. The presence of the active free adsorptive sites on the adsorbent surface results in fast adsorption of the dye from solution within the first 30 min.

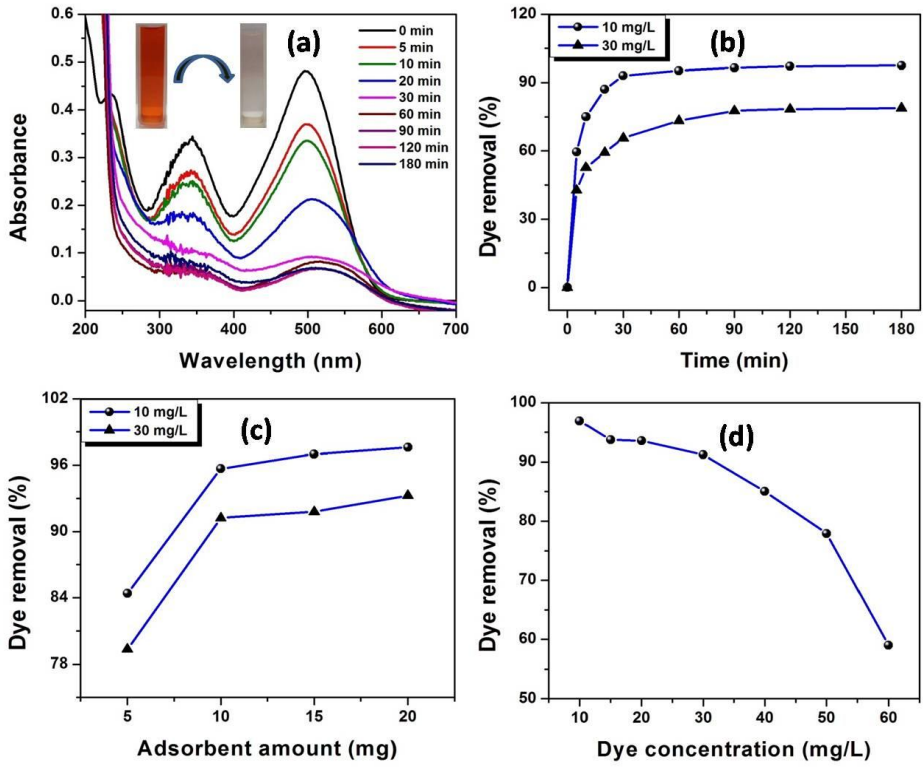

Figure 3C.5. (a) UV-vis spectra of CR on adsorption with different time (10 mg/L CR, 10 mg adsorbent), (b) effect of time (10 mg adsorbent), (c) effect of adsorbent amount (5–20 mg adsorbent) and (d) effect of initial dye concentrations (10–60 mg/L CR, 10 mg adsorbent) on adsorption of CR onto NiAl-S_1 LDH at T = 25 °C.

Figure 3C.5c shows the effect of adsorbent amount on adsorption process towards the removal of CR from aqueous solution. The adsorption experiment was carried out with 20

mL of 10 and 30 mg/L CR solutions and varying adsorbent amount in the ranges of 5–20 mg. A considerable increase in % dye removal of CR has been observed from 84.4 to 95.7% for 10 mg/L dye solution and from 79.3 to 91.2% for 30 mg/L dye solution with increase dosage of adsorbent from 5 to 10 mg. Again, on increasing the adsorbent amount upto 20 mg, no considerable increase in % dye removal of CR is observed (97.6 and 93.2% in case of 10 and 30 mg/L dye solutions, respectively). The adsorbent surface becomes saturated at higher concentration of adsorbent resulting in the lower in % dye removal. Moreover, aggregation of particles takes place at higher concentration of adsorbent through collision between the particles resulting in the decrease of surface area which increases the path length for diffusion [27]. Therefore, 10 mg is selected as an optimum adsorbent amount for further investigation. Figure 3C.5d displays the effect of initial dye concentration on the adsorption process. We carried out the study with a series of CR solutions with various concentrations in the range of 10–60 mg/L and 10 mg of the adsorbent (NiAl-S_1 LDH) for 60 min (equilibrium time). The % dye removal is decreased from 96.9 to 59.0% with increase in initial dye concentrations from 10 to 60 mg/L. This decrease in removal efficiency is because of the unavailability of the free active sites after the adsorption of a particular fixed quantity of dye concentration over the surface of the adsorbent.

The effect of solution pH on adsorption efficiency of NiAl-S_1 LDH towards the removal of CR has been investigated and results are shown in Figure 3C.6. We have done the experiment with two dye concentrations (10 and 30 mg/L) over the pH range of 2–10. The adsorbent amount used was 10 mg and volume of CR solution is 20 mL. For both cases it is observed that, the dye removal (%) is lower in the lower pH (pH<4) range. At lower pH, dissolution of the adsorbent materials results in the decrease of percentage dye removal. On increasing the solution pH from 4 to 6, the removal efficiency of CR increases, achieving a maximum % removal at pH 6. The enhanced adsorption efficiency of the adsorbent at pH 6 is attributed to the electrostatic attraction between the LDH adsorbent surface and anionic CR dye. Again, increase in the pH above 6, results in the decrease of dye removal (%) for both the cases. At higher pH, surface of the adsorbent becomes negatively charged and due to which electrostatic repulsion arises between the

anionic CR dye and surface of the adsorbent resulting in the lower in % removal [50]. Thus, we observed that NiAl-S_1 LDH shows good adsorption activity towards removal of CR at pH 6 and so further studies have been performed at this pH.

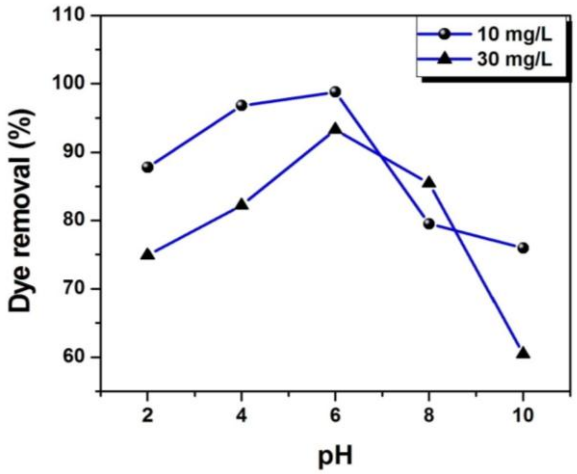

Figure 3C.6. Dye removal (%) of CR on NiAl-S_1 LDH at various pH ranges.

3C.1.4 Adsorption isotherms

The information regarding the affinity of adsorbates towards the adsorbent surfaces by distributing themselves between solid and liquid phase upon reaching an equilibrium position can be obtained with the help of adsorption isotherms [66]. The study was employed using 20 mL of each of the CR solutions with varying concentrations (10–60 mg/L) and a constant adsorbent amount (10 mg) under similar experimental conditions. Figure 3C.7a shows the isotherm plot for adsorptive removal of CR from aqueous solution using NiAl-S_1 LDH. The equilibrium adsorption capacity of the LDH goes on increasing with the equilibrium CR concentrations and reached the equilibrium position after complete coverage of the LDH surface. Figure 3C.7 (b and c) show the Langmuir and Freundlich adsorption isotherm plots for adsorptive removal of CR from aqueous solution by NiAl-S_1 LDH and the calculated parameters are summarized in Table 3C.2. The equilibrium isotherm data exhibits best fitting to the Langmuir model with correlation coefficient value almost unity (R^2 = 0.999), as compared to the Freundlich model (R^2 = 0.953) and thus prevails a monolayer adsorption process. The monolayer adsorption capacity, q_m for the adsorbent is 120.5 mg/g as calculated with the help of Langmuir

isotherm. The value is consistent with the experimental value, indicating the best fitting of adsorption data with the Langmuir isotherm. Table 3C.2 shows that the calculated R_L value in present study is 0.389 (R_L value between 0 and 1) and thereby confirming the favorable nature of the adsorption isotherm. The favorable nature of the adsorption process can also be depicted from the Freundlich constant, *n* and the value should lies in between 1 and 10. Here, the obtained *n* value 3 indicates a favorable adsorption of CR onto NiAl-S_1 LDH.

Table 3C.2. Langmuir, Freundlich and D-R adsorption isotherm parameters for adsorption of CR on NiAl-S_1 LDH.

Langmuir model				**Freundlich model**			**D-R model**			
q_m (mg/g)	b (L/mg)	R^2	R_L	n	k_F (mg/g) $(L/mg)^{1/n}$	R^2	q_e mg/g	β mol^2/kJ^2	E kJ/mol	R^2
120.5	0.346	0.999	0.389	3	40.4	0.953	99.6	0.528	1	0.977

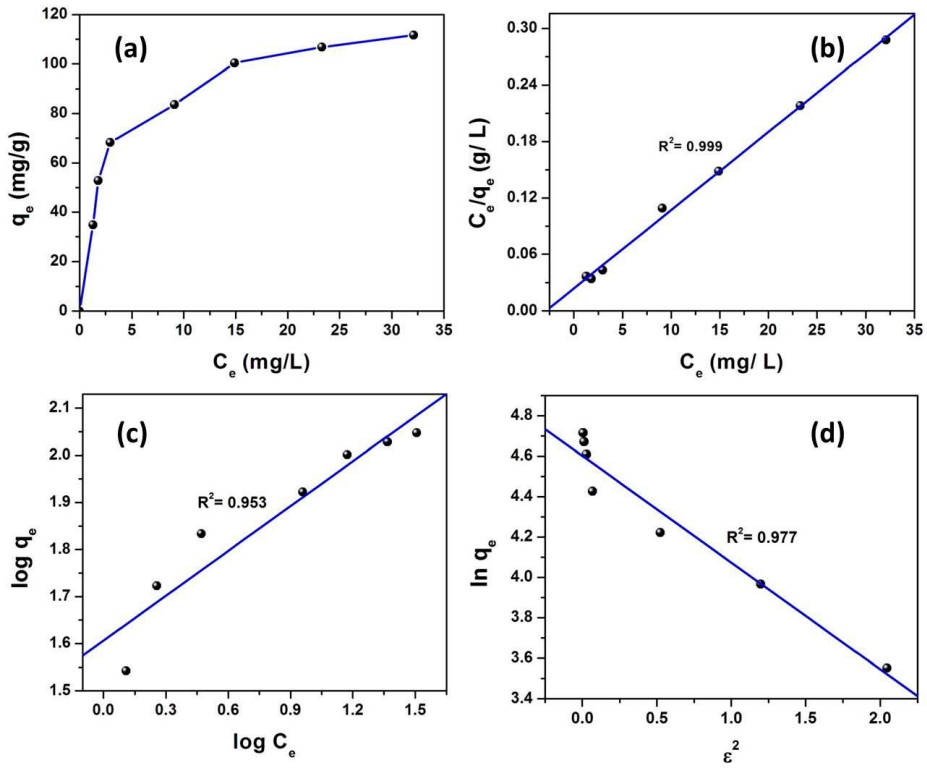

Figure 3C.7. (a) Adsorption isotherm, (b) Langmuir, (c) Freundlich and (d) D–R isotherm models for adsorption of CR on NiAl-S_1 LDH (10 mg adsorbent, T = 25 °C).

In addition, the isotherm data have been analyzed using Dubinin–Radushkevic (D–R) isotherm model in order to understand whether the nature of the adsorption process is physisorption or chemisorption. The isotherm parameters, β and q_e are obtained from the D–R isotherm plot of ln q_e versus ε^2 (Figure 3C.7d) and the values are summarized in Table 3C.2. The value of E determines the characteristics of the adsorption process, showing physical or chemical nature of the adsorption process. The E values between 1–16 kJ/mol denote a physical adsorption while the values above 16 kJ/mol signifies a chemisorption. In our study, the calculated E value for CR is 1 kJ/mol indicating that physisorption is the denominating one over the chemisorption process controlling the efficient removal of CR from aqueous solution by NiAl-S_1 LDH.

3C.1.5 Adsorption kinetics

To study the rate and the adsorption mechanism, the adsorption process was analysed by various adsorption kinetic models. We employed the study by using 20 mL of each of the CR solution (10 and 30 mg/L) and 10 mg of NiAl-S_1 LDH under similar experimental conditions. Figure 3C.8a shows the pseudo-first order kinetic plots for adsorptive removal of CR by NiAl-S_1 LDH for 10 and 30 mg/L dye concentrations. The rate constants and correlation coefficient (R^2) values have been calculated and presented in Table 3C.3. The R^2 values are 0.821 and 0.994 for 10 and 30 mg/L dye solutions, respectively. The second order kinetic model showed better R^2 values of 0.999 and 0.998 for 10 and 30 mg/L dye solutions, respectively (Figure 3C.8b, Table 3C.3). Thus the results show best fitting of kinetic data with the second order model signifying that the adsorption process follows a second order kinetics. The intraparticle diffusion kinetic study was employed for investigating the diffusion mechanism of the adsorption process for removal of CR by NiAl-S_1 LDH. The kinetic parameters, k_i and C are obtained from the plot of q_t versus $t^{1/2}$ (Figure 3C.8c) and the values are summarized in Table 3C.3. The plot is curved and also does not pass through the origin, indicating that more than one process have been involved as the rate limiting step in the adsorption process. The intraparticle diffusion mechanism is not the only rate limiting step. The external mass transfer plays a significant role for determining the rate limiting step of the adsorption process [5].

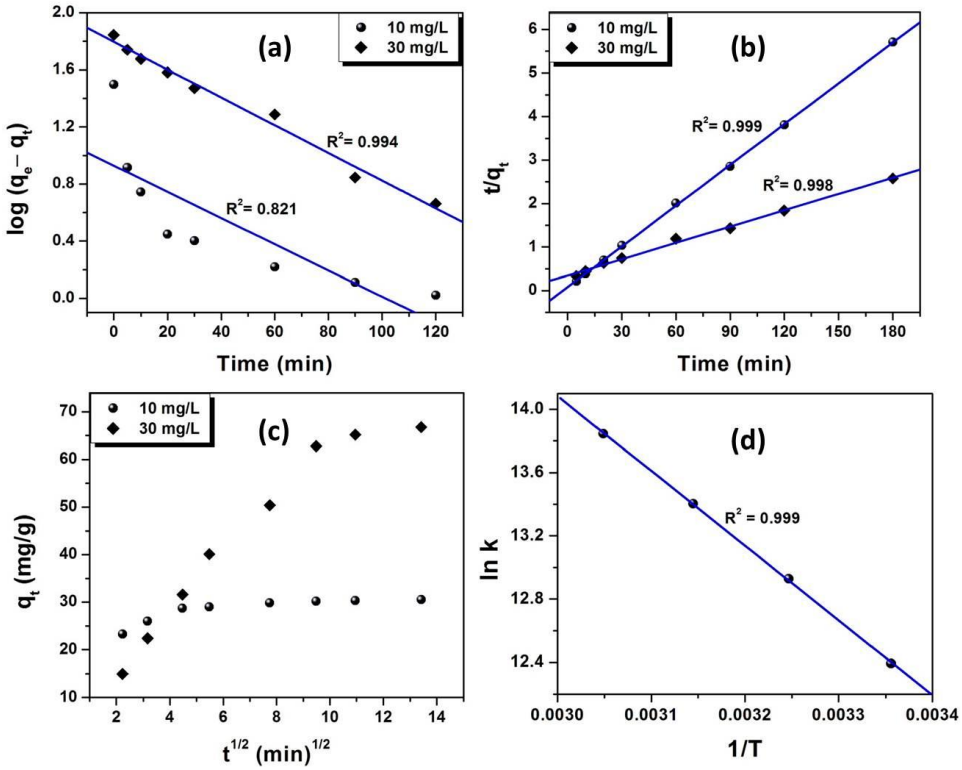

Figure 3C.8. (a) Pseudo-first order, (b) pseudo-second order, (c) intraparticle diffusion and (d) van't Hoff plot for adsorption of CR on NiAl-S_1 LDH (10 mg adsorbent).

Table 3C.3. Adsorption kinetic parameters for adsorptive removal of CR on NiAl-S_1 LDH.

Initial concentration of dye (C_o)	**Pseudo-first order**			**Pseudo-second order**		
mg/L	q_e (mg/g)	k_1 (min^{-1})	R^2	q_e (mg/g)	k_2 (g/mg·min)	R^2
10	8.4	0.0211	0.821	31.9	0.0160	0.999
30	62.4	0.0224	0.994	79.9	0.0005	0.998

3C.1.6 Adsorption thermodynamics study

Adsorption thermodynamics study was carried out to determine the influence of temperature on adsorption process considering various thermodynamic parameters like $\Delta G°$, $\Delta H°$ and $\Delta S°$. We carried out the experiment in temperature range of 25 to 55 °C

(298–328 K). Using k values obtained from the intercept of isotherm plot (C_e/q_e versus C_e) at different temperatures (data not shown), $\Delta G°$ values are calculated using equation 2.15 for CR adsorption by NiAl-S_1 LDH (Table 3C.4) [67–71]. Negative values of $\Delta G°$ for CR adsorption are observed at all the studied temperature and these negative values signify that the adsorption process is feasible and spontaneous in nature. Again, with increase in temperature, the $\Delta G°$ values become more negative, indicating that higher temperature favours the adsorption process. At higher temperature, the CR dye molecules gain sufficiently higher energy (kinetic energy) and thereby able to overcome the energy barrier restricting the bonding between the LDH adsorbent and CR molecules, reflecting energetically more favourable adsorption of CR by NiAl-S_1 LDH [14]. Figure 3C.8d shows the van't Hoff plot for CR adsorption by NiAl-S_1 (equation 2.17). The enthalpy change ($\Delta H°$) and entropy change ($\Delta S°$) values are calculated from the respective slope and intercept of the of ln k versus $1/T$ plot. The adsorption enthalpy change can determine whether the adsorption process is physical or chemical in nature. The values of $\Delta H°$ within the range of –20 to 40 kJ/mol correspond to the physical adsorption while the values within the range of –400 to –80 kJ/mol represent the chemisorption [27,72]. The value of $\Delta H°$ obtained is 39.2 kJ/mol, and that of $\Delta S°$ is 0.235 kJ/mol·K (Table 3C.4). The $\Delta H°$ value demonstrates that the adsorption process is physical in nature and the positive sign signifies the endothermic nature of adsorption. The positive value of $\Delta S°$ signifies increased randomness of the solid/liquid interface of the adsorbent material during the adsorption process and its low value signifies no remarkable change in entropy during the process [67,73].

Table 3C.4. Thermodynamic parameters for adsorptive removal of CR over NiAl-S_1 LDH.

Temperature (K)	$\Delta G°$ (kJ/mol)	$\Delta H°$ (kJ/mol)	$\Delta S°$ (kJ/mol·K)
298	–30.8	39.2	0.235
308	–33.2		
318	–35.5		
328	–37.8		

3C.1.7 Adsorption mechanism

The NiAl-S_1 LDH exhibits the efficient adsorption performance towards the removal of CR from aqueous solution. The adsorption mechanism has been investigated to understand the adsorption process clearly. The adsorption of CR by the LDH adsorbent can be understood in terms two pathways: (1) adsorption on the external surface and (2) anion exchange [74]. In the first path, adsorption occurs on the external surface of the adsorbent via the H-bonding and electrostatic attraction. In second path, intercalation of the dye molecule takes place in LDH structures via anion exchange between the interlayer anions and anions of the dye molecule [63]. Congo red (CR) is an anionic organic dye and contains negatively charged sulfonated group ($–SO_3^-$ Na^+) [75]. Therefore, electrostatic attraction arises between the negatively charged sulfonated group of CR dye and the LDH surface which favors the adsorption process towards the removal of CR. Also, formation of the H-bonding between the surface hydroxyl groups of the LDH and electronegative group of CR dye, aid in the enhanced adsorption performance of NiAl-S_1 LDH for removal CR from aqueous solution. Thus, the H-bonding and electrostatic attraction plays the major role in the adsorption mechanism for removal CR by NiAl-S_1 LDH. To understand the adsorption process further, XRD and SEM analyses of the LDH adsorbent have been carried out after CR adsorption. The XRD pattern shows that no characteristic changes arise on adsorption of CR dye as compared to the bare NiAl-S_1 LDH, showing that the LDH structure is retained after adsorption process and thus indicating physical nature of the adsorption process (Figure 3C.9).

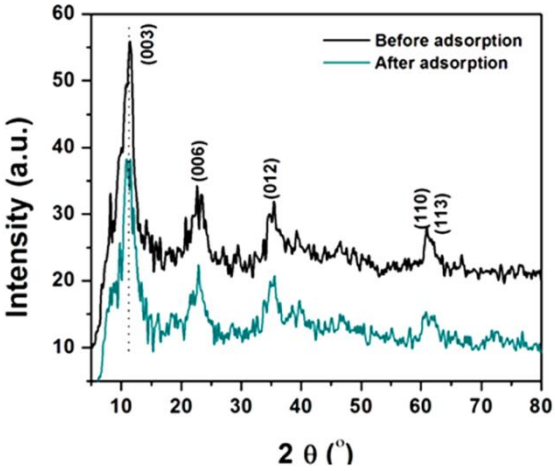

Figure 3C.9. XRD patterns of NiAl-S_1 LDH before and after adsorption of CR.

The SEM image shows that after adsorption the smooth surface of the LDH become rough with formation of a layer over the surface indicating the successful accumulation of CR dye on the surface NiAl-S_1 LDH (Figure 3C.10).

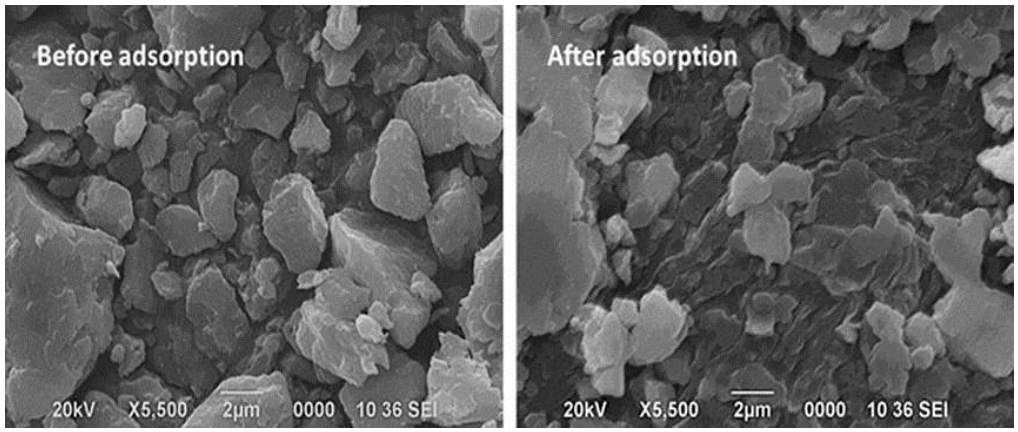

Figure 3C.10. SEM images of NiAl-S_1 LDH before and after adsorption of CR

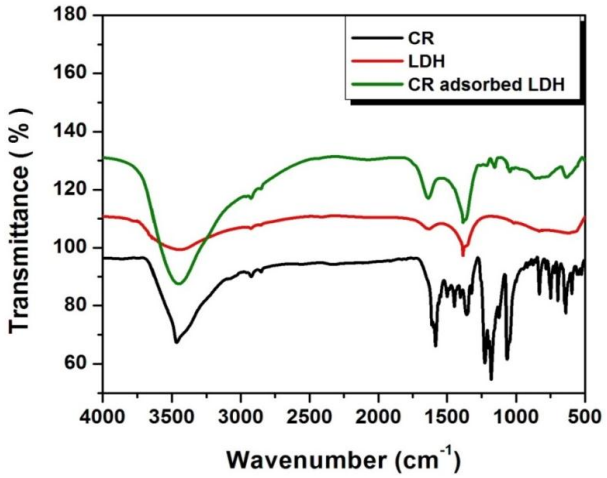

Figure 3C.11. FTIR spectra of CR, bare NiAl-S_1 LDH and CR adsorbed NiAl-S_1 LDH.

Furthermore, the interaction of CR dye onto the surface of NiAl-S_1 LDH can be understood well with the help of FTIR analysis. Figure 3C.11 shows the FTIR spectra of CR, bare NiAl-S_1 LDH and CR adsorbed NiAl-S_1 LDH. In the spectrum of CR, strong peaks can be observed around the wavelength region of 1000–1300 cm^{-1}, which is associated with the S=O stretching vibrations [76]. On adsorption over NiAl-S_1 LDH, these strong bands of CR get reduced and slightly broadened. The band due to –N=N– stretching vibration at around 1610 cm^{-1} gets diminished due to adsorption of CR over

LDH surface. The bands observed in the range of 850–1150 cm^{-1} are associated with the Si-O bands which on adsorption with LDH get reduced strongly.

Table 3C.5. Comparison of adsorption efficiency of NiAl-S_1 LDH for removal of CR with various reported adsorbents.

Entry	Adsorbents	Adsorbent dosage (mg)	C_0 (mg/L)	t (min)	% Dye removal	q_m (mg/g)	[Ref.]
1	NiAl-S_1 LDH	10	10	30	96.1	120.5	This Work
2	MgAl-LDH	50	20	20	–	111.1	[77]
3	NiO/GO nanosheets	50	20	180	99.6	123.9	[78]
4	Fe_3O_4@graphene nanocomposite	10	10	30	–	33.7	[79]
5	*p*TSA-Pani@GO-CNT	20	100	300	–	66.7	[80]
6	Anilinepropylsilica xerogel	0. 1 (g)	4-120	40	97	22. 6	[81]
7	Lignocellulosic Jute Fiber	10 (g/L)	15-30	50	99.9	27.1	[12]
8	Coir pith activated carbon	200	20	40	70	6.72	[82]
9	Activated red mud	8 (g/L)	10	90	85	7.08	[83]
10	Neem leaf powder	0.6 (g/L)	0.00287 (mmol/L)	300	99	41.2	[84]
11	Cellulosic waste orange peel	0.5 (g)	60	90	92	22.4	[85]
12	Chitosan hydrobeads	1 (g)	500	48 (h)	–	92.6	[86]
13	A*spergillus niger* biomass	0.2 (g)	50	30 (h)	–	14.2	[87]
14	AgNPs-coated AC	7 (g)	2	270	75	64.8	[88]
15	AuNPs-coated AC	7 (g)	2	270	88	71.1	[88]

Table 3C.5 shows the comparison of adsorption efficiency of NiAl-S_1 LDH for removal of CR with various reported adsorbents. Thus it is observed that NiAl-S_1 LDH is the efficient and potential adsorbent with high adsorption capacity towards the adsorptive removal of CR from aqueous solution.

Recyclability test of the used adsorbent (NiAl-S_1 LDH) was carried out and are presented in Figure 3C.12. Before the test, recovery of the adsorbent was first carried out by subjecting the used adsorbent with a solution of Na_2CO_3 and stirring for 24h. The adsorbent was then centrifuged, washed properly using distilled water and finally dried at 80 °C overnight. The recovered adsorbent was subjected to three more consecutive cycles with 10 mg/L CR and 10 mg adsorbent under similar adsorption parameters. The recovered adsorbent shows three successful cycles without any significant loss of the adsorption capacity. The figure shows 91, 86 and 80% removal for 1st, 2nd and 3rd cycle assuming 100% for the initial adsorption capacity of the adsorbent. Thus, NiAl-S_1 LDH is the highly potential adsorbent for removal of CR from aqueous solution with good recyclability.

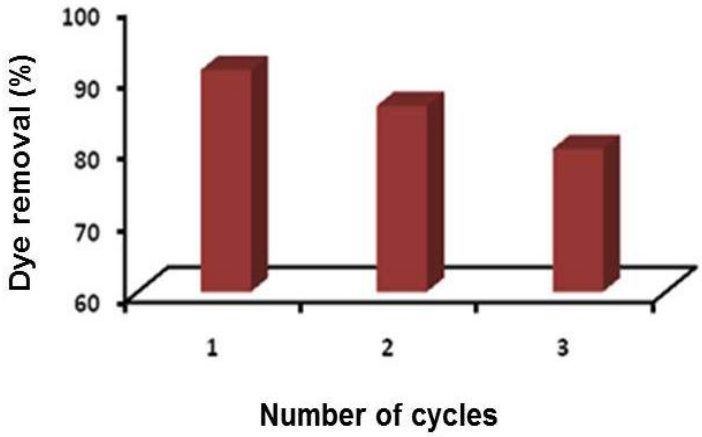

Figure 3C.12. Dye removal (%) of CR with number of cycles on NiAl-S_1 LDH (10 mg/L CR, 10 mg adsorbent, T = 25 °C).

In summary, we have synthesized NiAl LDH by using co-precipitation method followed by ultrasonic irradiation for various irradiation time and the resulting materials have been employed for the adsorptive removal of congo red (CR) from aqueous solution. The powder XRD patterns reveal the formation of LDHs that exhibits sharp, intense peak

at low 2θ angles and broad as well as less intense peaks at higher 2θ angles. NiAl-S_1 LDH synthesized at 1h ultrasonic irradiation time exhibits efficient adsorption capacity for removal of CR compared to the LDH synthesized under normal reflux condition. The effects of various parameters such as ultrasonic irradiation time, contact time, adsorbent dosage and initial dye concentration on the adsorption capacity of CR onto NiAl LDH materials have been studied thoroughly. The equilibrium adsorption data are fitted well with Langmuir isotherm model, indicating monolayer adsorption of CR over NiAl-LDH with adsorption capacity of 120.5 mg/g at pH 6. The adsorption kinetics study shows that the adsorption process followed pseudo-second order kinetics. The thermodynamic study reveals feasible and spontaneous nature of the adsorption process. The change in value of adsorption enthalpy also reflects the physical and endothermic nature of the adsorption process.

REFERENCES

[1] Liu, F., Leung, Y. H., Djurisic, A. B., Ng, A. M. C., and Chan, W. K. Native defects in ZnO: Effect on dye adsorption and photocatalytic degradation. *The Journal of Physical Chemistry C*, 117(23):12218–12228, 2013.

[2] Yang, L., Qian, L., Feng, Y., Tang, P., and Li, D. Acid blue 129 and salicylate cointercalated layered double hydroxides: Assembly, characterization, and photostability. *Industrial & Engineering Chemistry Research*, 53(46):17961–17967, 2014.

[3] Géraud, E., Bouhent, M., Derriche, Z., Leroux, F., Prévot, V., and Forano, C. Texture effect of layered double hydroxides on chemisorption of orange II. *Journal of Physics and Chemistry of Solids*, 68(5–6):818–823, 2007.

[4] Yang, Z., Ji, S., Gao, W., Zhang, C., Ren, L., Tjiu, W. W., and Liu, T. Magnetic nanomaterial derived from graphene oxide/layered double hydroxide hybrid for efficient removal of methyl orange from aqueous solution. *Journal of colloid and interface science*, 408:25–32, 2013.

[5] Ai, L., Zhang, C., and Meng, L. Adsorption of methyl orange from aqueous solution on hydrothermal synthesized Mg-Al layered double hydroxide. *Journal of Chemical Engineering Data*, 56(11):4217–4225, 2011.

[6] Jia, Z., Li, Z., Li, S., Li, Y., and Zhu, R. Adsorption performance and mechanism of methylene blue on chemically activated carbon spheres derived from hydrothermally-prepared poly(vinyl alcohol) microspheres. *Journal of Moecular Liquids*, 220:56–62, 2016.

[7] Liu, Y., Zeng, G., Tang, L., Cai, Y., Pang, Y., Zhang, Y., Yang, G., Zhou, Y., He, X., and He, Y. Highly effective adsorption of cationic and anionic dyes on magnetic Fe/Ni nanoparticles doped bimodal mesoporous carbon. *Journal of Colloid and Interface Science.* 448:451–459, 2015.

[8] Ai, L., Zhou, Y., and Jiang, J. Removal of methylene blue from aqueous solution by montmorillonite/$CoFe_2O_4$ composite with magnetic separation performance. *Desalination*, 266(1–3):72–77, 2011.

[9] Zhang, T., Huang, X., and Asefa, T. Nanostructured polymers with high surface area using inorganic templates for the efficient extraction of anionic dyes from solutions. *Chemical Communications*, 51:16135–16138, 2015.

[10] Munagapati, V. S. and Kim, D. -S. Adsorption of anionic azo dye congo red from aqueous solution by cationic modified orange peel powder. *Journal of Molecular Liquids*, 220:540–548, 2016.

[11] Zhu, S., Jiao, S., Liu, Z., Pang, G., and Feng, S. High adsorption capacity for dye removal by CuZn hydroxyl double salts. *Environmental Science: Nano*, 1:113–121, 2014.

[12] Roy, A., Adhikari, B., and Majumder, S. B. Equilibrium, kinetic and thermodynamic studies of azo dye adsorption from aqueous solution by chemically modified lignocellulosic jute fiber. *Industrial & Engineering Chemistry Research*, 52(19):6502−6512, 2013.

[13] Ma, J., Yu, F., Zhou, L., Jin, L., Yang, M., Luan, J., Tang, Y., Fan, H., Yuan, Z., and Chen, J. Enhanced adsorptive removal of methyl orange and methylene blue from aqueous solution by alkali-activated multiwalled carbon nanotubes. *ACS Applied Material & Interfaces*, 4(11):5749–5760, 2012.

[14] Pahalagedara, M. N., Samaraweera, M., Dharmarathna, S., Kou, C. -H., Pahalagedara, L. R., Gascón, J. A., and Suib, S. L. Removal of azo dyes: Intercalation into sonochemically synthesized NiAl layered double hydroxide. *The Journal of Physical Chemistry C*, 118(31):17801–17809, 2014.

[15] Cheng, R., Ou, S., Xiang, B., Li, Y., and Liao, Q. Equilibrium and molecular mechanism of anionic dyes adsorption onto copper (II) complex of dithiocarbamate-modified starch. *Langmuir*, 26(2):752–758, 2010.

[16] Mittal, A., Mittal, J., Malviya, A., Kaur, D., and Gupta, V. K. Adsorption of hazardous dye crystal violet from wastewater by waste materials. *Journal of Colloid and Interface Science*, 343(2):463–473, 2010.

[17] Zhang, W., Yang, H., Dong, L., Yan, H., Li, H., Jiang, Z., and Kan, X. Efficient removal of both cationic and anionic dyes from aqueous solutions using a novel amphoteric straw-based adsorbent. *Carbohydrate Polymers*, 90(2):887–893, 2012.

[18] Amuda, O. S. and Amoo, I. A. Coagulation/flocculation process and sludge conditioning in beverage industrial wastewater treatment. *Journal of Hazardous Materials*, 141(3):778–783, 2007.

[19] Ksibi, M. Chemical oxidation with hydrogen peroxide for domestic wastewater treatment. *Chemical Engineering Journal*, 119(2–3):161–165, 2006.

[20] El-Sheekh, M. M., Gharieb, M. M., and Abou-El-Souod, G. W. Biodegradation of dyes by some green algae and cyanobacteria. *International Biodeterioration & Biodegradation*, 63(6):699–704, 2009.

[21] Heinfling, A., Bergbauer, M., and Szewzyk, U. Biodegradation of azo and phthalocyanine dyes by *Trametes versicolor* and *Bjerkandera adusta*. *Applied Microbiology and Biotechnology*, 48(2):261–266, 1997.

[22] Aksu, Z. and Tezer, S. Biosorption of reactive dyes on the green alga *Chlorella vulgaris*. *Process Biochemistry*, 40(3):1347–1361, 2005.

[23] Xia, S. -J., Liu, F. -X., Ni, Z. -M., Xue, J. -L., and Qian, P. -P. Layered double hydroxides as efficient photocatalysts for visible-light degradation of rhodamine B. *Journal of Colloid and Interface Science*, 405:195–200, 2013.

[24] Zhao, Y., Wei, M., Lu, J., Wang, Z. L., and Duan, X. Biotemplated hierarchical nanostructure of layered double hydroxides with improved photocatalysis performance. *ACS Nano*, 3(12):4009–4016, 2009.

[25] Parida, K. M. and Mohapatra, L. Carbonate intercalated Zn/Fe layered double hydroxide: A novel photocatalyst for the enhanced photo degradation of azo dyes. *Chemical Engineering Journal*, 179:131–139, 2012.

[26] Chen, J., Feng, J., and Yan, W. Influence of metal oxides on the adsorption characteristics of PPy/metal oxides for methylene blue, *Journal of Colloid and Interface Science*, 475:26–35, 2016.

[27] Zaghouane-Boudiaf, H., Boutahala, M., and Arab, L. Removal of methyl orange from aqueous solution by uncalcined and calcined MgNiAl layered double hydroxides (LDHs). *Chemical Engineering Journal*, 187:142–149, 2012.

[28] Shou, J., Jiang, C., Wang, F., Qiu, M., and Xu, Q. Fabrication of Fe_3O_4/MgAl-layered double hydroxide magnetic composites for the effective decontamination

of Co (II) from synthetic wastewater. *Journal of Molecular Liquids*, 207:216–223, 2015.

[29] Ghorai, S., Sarkar, A., Raoufi, M., Panda, A. B., Schönherr, H., and Pal, S. Enhanced removal of methylene blue and methyl violet dyes from aqueous solution using a nanocomposite of hydrolyzed polyacrylamide grafted xanthan gum and incorporated nanosilica. *ACS Applied Materials & Interfaces*, 6(7):4766–4777, 2014.

[30] Gupta, V. K., Jain, R., Siddiqui, M. N., Saleh, T. A., Agarwal, S., Malati, S., and Pathak, D. Equilibrium and thermodynamic studies on the adsorption of the dye rhodamine-B onto mustard cake and activated carbon. *Journal of Chemical & Engineering Data*, 55(11):5225–5229, 2010.

[31] Sun, D., Zhang, X., Wu, Y., and Liu, X. Adsorption of anionic dyes from aqueous solution on fly ash. *Journal of Hazardous Materials*, 181(1–3):335–342, 2010.

[32] Kyzas, G. Z., Kostoglou, M., and Lazaridis, N. K. Relating interactions of dye molecules with chitosan to adsorption kinetic data. *Langmuir*, 26(12):9617–9626, 2010.

[33] Travlou, N. A., Kyzas, G. Z., Lazaridis, N. K., and Deliyanni, E. A. Functionalization of graphite oxide with magnetic chitosan for the preparation of a nanocomposite dye adsorbent. *Langmuir*, 29(5):1657−1668, 2013.

[34] Wang, S., Li, H., and Xu, L. Application of zeolite MCM-22 for basic dye removal from wastewater. *Journal of Colloid and Interface Science*, 295(1):71–78, 2006.

[35] Ma, Y. -L., Xu, Z. -R., Guo, T., and You, P. Adsorption of methylene blue on Cu (II)-exchanged montmorillonite. *Journal of Colloid and Interface Science*, 280(2):283–288, 2004.

[36] Karaoğlu, M. H., Doğan, M., and Alkan, M. Removal of reactive blue 221 by kaolinite from aqueous solutions. *Industrial & Engineering Chemistry Research*, 49(4):1534–1540, 2010.

[37] Aladağ, E., Fil, B. A., Boncukcuoğlu, R., Sözüdoğru, O., and Yılmaz, A. E. Adsorption of methyl violet dye, a textile industry effluent onto montmorillonite—

batch study. *Journal of Dispersion Science and Technology*, 35(12):1737–1744, 2014.

[38] Zhang, C., Yang, S., Chen, H., He, H., and Sun, C. Adsorption behavior and mechanism of reactive brilliant red X-3B in aqueous solution over three kinds of hydrotalcite-like LDHs. *Applied Surface Science*, 301:329–337, 2014.

[39] Extremera, R., Pavlovic, I., Pérez, M. R., and Barriga, C. Removal of acid orange 10 by calcined Mg/Al layered double hydroxides from water and recovery of the adsorbed dye. *Chemical Engineering Journal*, 213:392–400, 2012.

[40] He, S., Zhao, Y., Wei, M., Evans, D. G., and Duan, X. Fabrication of hierarchical layered double hydroxide framework on aluminium foam as a structured adsorbent for water treatment. *Industrial & Engineering Chemistry Research*, 51(1):285–291, 2012.

[41] Wang, G., Yang, M., Li, Z., Lin, K., Jin, Q., Xing, C., Hu, Z., and Wang, D. Synthesis and characterization of Zn-doped MgAl-layered double hydroxide nanoparticles as PVC heat stabilizer. *Journal of Nanoparticle Research*, 1:1882–1889, 2013.

[42] Parida, K., Mohapatra, L., and Baliaarsingh, N. Effect of Co^{2+} substitution in the framework of carbonate intercalated Cu/Cr LDH on structural, electronic, optical, and photocatalytic properties. *The Journal of Physical Chemistry C*, 116(42):22417–22424, 2012.

[43] Mandal, S., Tichit, D., Lerner, D. A., and Marcotte, N. Azoic dye hosted in layered double hydroxide: Physicochemical characterization of the intercalated materials. *Langmuir*, 25(18):10980–10986, 2009.

[44] Kloprogge, J. T., Wharton, D., Hickey, L., and Frost, R. L. Infrared and Raman study of interlayer anions CO_3^{2-}, NO_3^-, SO_4^{2-} and ClO_4^- in Mg/Al hydrotalcite. *American Mineralogist*, 87(5–6):623–629, 2002.

[45] Kloprogge, J. T. and Frost, R. L. Fourier transform infrared and Raman spectroscopic study of the local structure of Mg-, Ni-, and Co-hydrotalcites. *Journal of Solid State Chemistry*, 146(2):506–515, 1999.

[46] Kagunya, W., Baddour-Hadjean, R., Kooli, F., and Jones, W. Vibrational modes in layered double hydroxides and their calcined derivatives. *Chemical Physics*, 236(1–3):225–234, 1998.

[47] Kloprogge, J. T. and Frost, R. L. Infrared and Raman spectroscopic studies of layered double hydroxides (LDHs). In Rives, V., editor, *Layered Double Hydroxides: Present and Future*, pages 153–215, ISBN: 1-59033-060-9. Nova Science Publishers, New York, 2006.

[48] Baliarsingh, N., Parida, K. M., and Pradhan, G. C. Effects of Co, Ni, Cu, and Zn on photophysical and photocatalytic properties of carbonate intercalated M^{II}/Cr LDHs for enhanced photodegradation of methyl orange. *Industrial & Engineering Chemistry Research*, 53(10):3834–3841, 2014.

[49] Auxilio, A. R., Andrews, P. C., Junk, P. C., Spiccia, L., Neumann, D., Raverty, W., and Vanderhoek, N. Adsorption and intercalation of acid blue 9 on Mg–Al layered double hydroxides of variable metal composition. *Polyhedron*, 26(14):3479–3490, 2007.

[50] Saha, B., Das, S., Saikia, J., and Das, G. Preferential and enhanced adsorption of different dyes on iron oxide nanoparticles: A comparative study. *The Journal of Physical Chemistry C*, 115(16):8024–8033, 2011.

[51] Liu, Y., Tian, Y., Luo, C., Cui, G., and Yan, S. One-pot preparation of a MnO_2–graphene–carbon nanotube hybrid material for the removal of methyl orange from aqueous solutions. *New Journal of Chemistry*, 39:5484–5492, 2015.

[52] Annadurai, G., Juang, R. -S., and Lee, D. -J. Use of cellulose-based wastes for adsorption of dyes from aqueous solutions. *Journal of Hazardous Materials*, 92(3):263–274, 2002.

[53] Iida, Y., Kozuka, T., Tuziuti, T., and Yasui, K. Sonochemically enhanced adsorption and degradation of methyl orange with activated aluminas. *Ultrasonics*, 42(1–9):635–639, 2004.

[54] Liu, R., Fu, K., Zhang, B., Mei, D., Zhang, H., and Liu, J. Removal of methyl orange by modified halloysite nanotubes. *Journal of Dispersion Science and Technology*, 33(5):711–718, 2012.

[55] Pal, J., Deb, M. K., Deshmukh, D. K., and Verma, D. Removal of methyl orange by activated carbon modified by silver nanoparticles. *Applied Water Science*, 3(2):367–374, 2013.

[56] Kannan, S., Dubey, A., and Knozinger, H. Synthesis and characterization of CuMgAl ternary hydrotalcites as catalysts for the hydroxylation of phenol. *Journal of Catalysis*, 231(2):381–392, 2005.

[57] Valente, J. S., Hernandez-Cortez, J., Cantu, M. S., Ferrat, G., and López-Salinas, E. Calcined layered double hydroxides Mg–Me–Al (Me: Cu, Fe, Ni, Zn) as bifunctional catalysts. *Catalysis Today*, 150(3–4):340–345, 2010.

[58] Bharali, D. and Deka, R. C. Adsorptive removal of congo red from aqueous solution by sonochemically synthesized NiAl layered double hydroxide. *Journal of Environmental Chemical Engineering* 5(2):2056–2067, 2017.

[59] Malik, R., Ramteke, D. S., and Wate, S. R. Physico-chemical and surface characterization of adsorbent prepared from groundnut shell by $ZnCl_2$ activation and its ability to adsorb colour. *Indian Journal of Chemical Technology*,13:319–328, 2006.

[60] Kovanda, F., Jirátová, K., Rymeš, J., and Koloušek, D. Characterization of activated Cu/Mg/Al hydrotalcites and their catalytic activity in toluene combustion. *Applied Clay Science*, 18(1–2):71–80, 2001.

[61] Bharali, D., Devi, R., Bharali, P., and Deka, R. C. Synthesis of high surface area mixed metal oxide from the NiMgAl LDH precursor for nitro-aldol condensation reaction. *New Journal of Chemistry*, 39:172−178, 2015.

[62] Xu, H., Zeiger, B. W., and Suslick, K. S. Sonochemical synthesis of nanomaterials. *Chemical Society Reviews*, 42(7):2555−2567, 2013.

[63] Lei, C., Pi, M., Kuang, P., Guo, Y., and Zhang, F. Organic dye removal from aqueous solutions by hierarchical calcined Ni-Fe layered double hydroxide: Isotherm, kinetic and mechanism studies. *Journal of Colloid and Interface Science*, 496:158−166, 2017.

[64] Li, F., Jiang, X., Evans, D. G., and Duan, X. Structure and basicity of mesoporous materials from Mg/Al/In layered double hydroxides prepared by separate

nucleation and aging steps methods. *Journal of Porous Materials*, 12(1):55−63, 2005.

[65] Bang, J. H. and Suslick, K. S. Applications of ultrasound to the synthesis of nanostructured materials. *Advanced Materials*, 22(10):1039−1059, 2010.

[66] Zhang, M., Yao, Q., Lu, C., Li, Z., and Wang, W. Layered double hydroxide–carbon dot composite: High-performance adsorbent for removal of anionic organic dye. *ACS applied materials & interfaces*, 6(22):20225–20233, 2014.

[67] Liu, Y. Is the free energy change of adsorption correctly calculated?. *Journal of Chemical & Engineering Data*, 54(7):1981–1985, 2009.

[68] Liu, Y. and Liu, Y. J. Biosorption isotherms, kinetics and thermodynamics. *Separation and Purification Technology*, 61(3):229–242, 2008.

[69] Liu, Y. and Xu, H. Equilibrium, thermodynamics and mechanisms of Ni^{2+} biosorption by aerobic granules. *Biochemical Engineering Journal*, 35(2):174–182, 2007.

[70] Lima, É. C., Adebayo, M. A., and Machado, F. M. Kinetic and equilibrium models of adsorption. In Bergmann, C. P., and Machado F. M., editors, *Carbon Nanomaterials as Adsorbents for Environmental and Biological Applications*, pages 33–69, Springer International Publishing, New York, 2015.

[71] Aksu, Z. Determination of the equilibrium, kinetic and thermodynamic parameters of the batch biosorption of nickel (II) ions onto *Chlorella vulgaris*. *Process Biochemistry*, 38(1):89–99, 2002.

[72] Abdelkader, N. B. H., Bentouami, A., Derriche, Z., Bettahar, N., and De Menorval, L. C. Synthesis and characterization of Mg–Fe layer double hydroxides and its application on adsorption of orange G from aqueous solution. *Chemical Engineering Journal*, 169(1–3):231–238, 2011.

[73] Vimonses, V., Lei, S., Jin, B., Chow, C. W., and Saint, C. Kinetic study and equilibrium isotherm analysis of congo red adsorption by clay materials. *Chemical Engineering Journal*, 148(2–3):354–364, 2009.

[74] Li, B., Zhang, Y., Zhou, X., Liu, Z., Liu, Q., and Li, X. Different dye removal mechanisms between monodispersed and uniform hexagonal thin plate-like

$MgAl–CO_3^{2–}$-LDH and its calcined product in efficient removal of congo red from water. *Journal of Alloys and Compounds*, 673:265–271, 2016.

[75] Chatterjee, S., Chatterjee, S., Chatterjee, B. P., and Guha, A. K. Adsorptive removal of congo red, a carcinogenic textile dye by chitosan hydrobeads: Binding mechanism, equilibrium and kinetics. *Colloids and Surfaces A: Physicochemical and Engineering Aspects*, 299(1–3):146–152, 2007.

[76] Acemio˘glu, B. Adsorption of congo red from aqueous solution onto calcium-rich fly ash. *Journal of Colloid and Interface Science*, 274(2):371–379, 2004.

[77] Lafi, R., Charradi, K., Djebbi, M. A., Amara, A. B. H., and Hafiane, A. Adsorption study of congo red dye from aqueous solution to Mg–Al–layered double hydroxide. *Advanced Powder Technology*, 27(1):232–237, 2016.

[78] Rong, X., Qiu, F., Qin, J., Zhao, H., Yan, J., and Yang, D. A facile hydrothermal synthesis, adsorption kinetics and isotherms to congo red azo-dye from aqueous solution of NiO/graphene nanosheets adsorbent. *Journal of Industrial and Engineering Chemistry*, 26:354–363, 2015.

[79] Yao, Y., Miao, S., Liu, S., Ma, L. P., Sun, H., and Wang, S. Synthesis, characterization, and adsorption properties of magnetic Fe_3O_4@graphene nanocomposite. *Chemical Engineering Journal*, 184:326–332, 2012.

[80] Ansari, M. O., Kumar, R., Ansari, S. A., Ansari, S. P., Barakat, M. A., Alshahrie, A., and Cho, M. H. Anion selective pTSA doped polyaniline@graphene oxide-multiwalled carbon nanotube composite for Cr (VI) and congo red adsorption. *Journal of Colloid and Interface Science*, 496:407−415, 2017.

[81] Pavan, F. A., Dias, S. L. P., Lima, E. C., and Benvenutti, E. V. Removal of congo red from aqueous solution by anilinepropylsilica xerogel. *Dyes and Pigments*, 76(1):64−69, 2008.

[82] Namasivayam, C. and Kavitha, D. Removal of congo red from water by adsorption onto activated carbon prepared from coir pith, an agricultural solid waste. *Dyes and Pigments*, 54(1):47–58, 2002.

[83] Tor, A. and Cengeloglu, Y. Removal of congo red from aqueous solution by adsorption onto acid activated red mud, *Journal of Hazardous Materials*, 138(2):409–415, 2006.

[84] Bhattacharyya, K. G. and Sharma, A. *Azadirachta indica* leaf powder as an effective biosorbent for dyes: A case study with aqueous congo red solutions. *Journal of Environmental Management*, 71(3):217–229, 2004.

[85] Namasivayam, C., Muniasamy, N., Gayathri, K., Rani, M., and Ranganathan, K. Removal of dyes from aqueous solutions by cellulosic waste orange peel. *Bioresource Technology*, 57(1):37–43, 1996.

[86] Chatterjee, S., Chatterjee, S., Chatterjee, B. P., and Guha, A. K. Adsorptive removal of congo red, a carcinogenic textile dye by chitosan hydrobeads: Binding mechanism, equilibrium and kinetics. *Colloids and Surfaces A: Physicochemical and Engineering Aspects*, 299(1):146–152, 2007.

[87] Fu, Y. and Viraraghavan, T. Removal of congo red from an aqueous solution by fungus *Aspergillus niger*. *Advances in Environmental Research*, 7(1):239–247, 2002.

[88] Pal, J. and Deb, M. K. Efficient adsorption of congo red dye from aqueous solution using green synthesized coinage nanoparticles coated activated carbon beads. *Applied Nanoscience*, 4(8):967–978, 2014.